buildings

MDPI

Article

Hydrothermal Performance of Conventional Inclined and Base-Arranged Novel Horizontal Two-Phase Closed Thermosyphons in a Wide Asphalt Embankment Under Permafrost Warming

Juncheng Wang [1,2], Ji Chen [1,*], Tianchun Dong [3], Shouhong Zhang [3], Xin Hou [1], Jingyi Zhao [1], Qihang Mei [1,4] and Yingmei Wang [5]

[1] Qinghai-Beiluhe Plateau Frozen Soil Engineering Safety National Observation and Research Station, The State Key Laboratory of Cryospheric Science and Frozen Soil Engineering, Northwest Institute of Eco-Environment and Resources, Chinese Academy of Sciences, Lanzhou 730000, China; wangjuncheng@nieer.ac.cn (J.W.); houxin@nieer.ac.cn (X.H.); zhaojingyi@lzb.ac.cn (J.Z.); meiqh@lzb.ac.cn (Q.M.)
[2] University of Chinese Academy of Sciences, Beijing 100049, China
[3] China Railway Qinghai Tibet Grp Co., Ltd., Xining 810007, China; dongtianchun@163.com (T.D.); vicky_19@126.com (S.Z.)
[4] Ningbo Housing Safety and Property Management Center (Ningbo Termite Control Center), Ningbo 315100, China
[5] School of Green Energy and Storage, Lanzhou University of Technology, Lanzhou 730050, China; wangyingmei@lut.edu.cn
* Correspondence: chenji@lzb.ac.cn

Abstract

Climate warming, pavement heat storage and lateral heat intrusion accelerate active-layer deepening and uneven thaw settlement along permafrost transportation corridors. In wide asphalt embankments, heat is stored across a broad pavement-embankment section, while slope-aspect solar input drives asymmetric thermal erosion toward the sunny-side toe. Existing embankments protected by two-phase closed thermosyphons (TPCTs) are commonly evaluated by temperature reduction, maximum thaw depth or local cooling efficiency, but these metrics do not describe frozen-state continuity or residual weak zones. This study develops a three-dimensional hydrothermal model to compare a no-TPCT reference embankment, a conventional inclined TPCT layout and a base-arranged novel horizontal TPCT layout under long-term regional warming. Without TPCTs, the year-20 thaw depth reached 10.06 m at the sunny-side shoulder and 9.76 m beneath the centerline, with thermal disturbance propagating toward the sunny-side toe. Both TPCT layouts stabilized the 0 °C isotherm beneath the embankment. The inclined layout generated deep localized cooling, whereas the horizontal layout formed a more continuous shallow frozen zone, with longer operating durations and year-20 annual cumulative cooling capacities of 1870 and 1600 MJ on the sunny and shaded sides, respectively. The findings support an assessment based on frozen-state continuity, cross-sectional temperature uniformity and residual weak-zone development. Base-arranged novel horizontal TPCTs are better suited to shallow continuity, whereas inclined TPCTs remain useful for deep localized cooling.

Keywords: permafrost; two-phase closed thermosyphon; wide asphalt embankment; climate warming; hydrothermal modelling; frozen-state continuity; residual weak zone

Check for updates

Academic Editor: Salvatore Verre

Received: 2 June 2026
Revised: 22 June 2026
Accepted: 24 June 2026
Published: 25 June 2026

Copyright: © 2026 by the authors. Licensee MDPI, Basel, Switzerland. This article is an open access article distributed under the terms and conditions of the Creative Commons Attribution (CC BY) license.

1. Introduction

Permafrost regions support major transportation corridors in high-latitude and high-altitude cold regions. Because ice–water phase composition, pore-water migration and soil stiffness change rapidly near the freezing point, permafrost is sensitive to climate warming and engineering disturbance [1–4]. These changes can cause active-layer deepening, thaw settlement, frost heave, pavement cracking and slope deformation [2,5,6]. Wide asphalt embankments are especially vulnerable because dark pavements absorb solar radiation and the embankment body stores heat across a large cross-section. Slope-aspect differences further promote uneven heat input, making long-term frozen-ground protection a central construction problem in permafrost regions [7–9].

To limit heat transfer into underlying permafrost, engineering has adopted several cooling measures. Crushed-rock revetments and berms enhance cold-season convective cooling, ventilation ducts promote air circulation, insulation layers reduce downward heat flux and sunshades modify surface energy balance [10–15]. Two-phase closed thermosyphons (TPCTs) have been widely used as active heat-transfer devices that transfer heat from the ground to the atmosphere [16–19]. As shown in Figure 1, the buried evaporator absorbs ground heat, vapor transports heat upward inside TPCTs, the condenser releases heat to ambient air, and condensate returns to the evaporator by gravity [16,19]. In practice, these measures are combined because each controls a different part of the embankment-ground energy pathway [15,20,21]. In wide asphalt embankments, however, residual weak zones may remain near shoulders or slope toes because heat accumulation, water migration and slope-aspect effects interact [8,9,22].

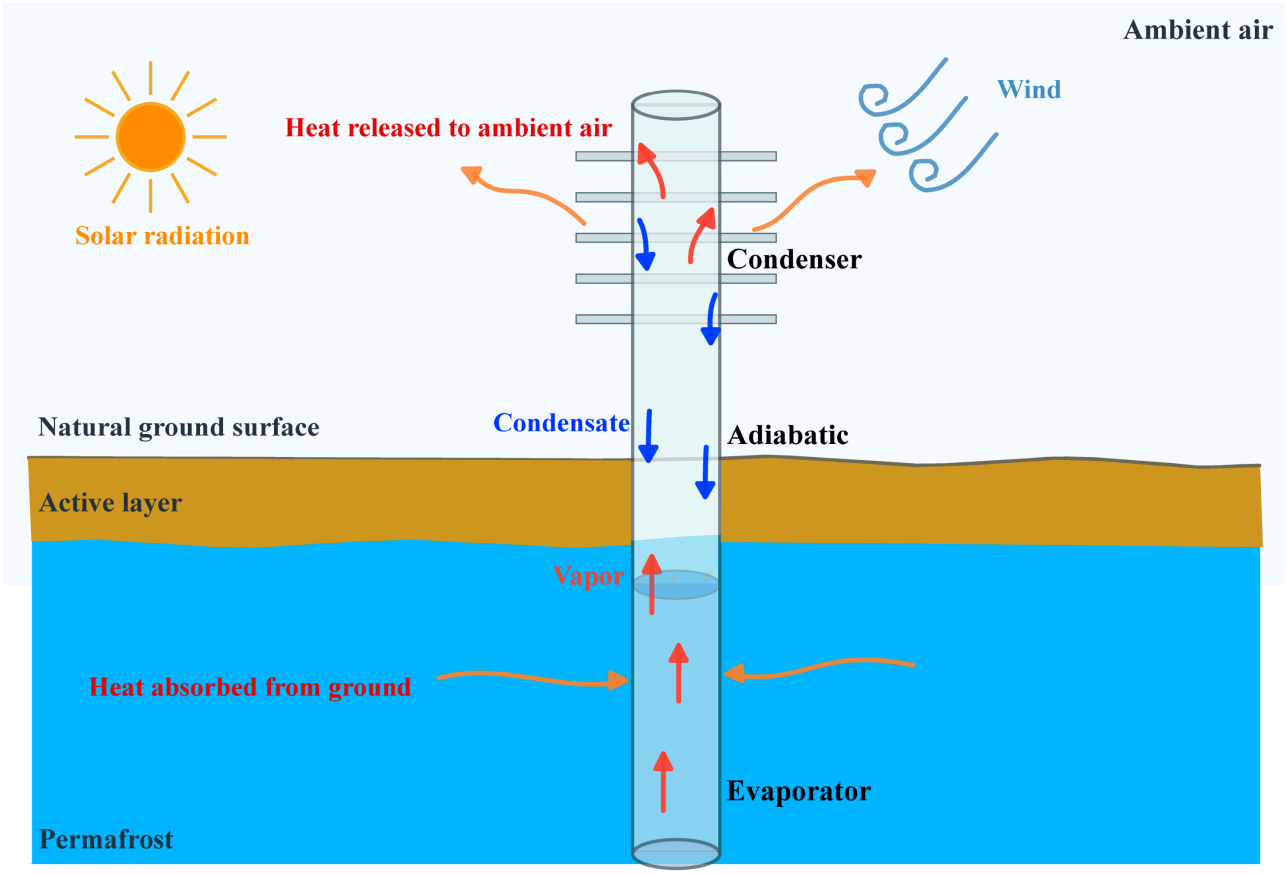


Figure 1. Working principle of a two-phase closed thermosyphon (TPCT) in permafrost regions.

TPCT embankments have been studied as field-scale measures for slowing ground warming and reducing thaw-related deformation. Long-term monitoring shows that TPCTs operate mainly during the cold season, form low-temperature zones around evaporators and raise or maintain the permafrost table [17–19]. Part of this cooling can persist through the warm season and accumulate over multiple years in wide asphalt embankments. Embankment response, however, is not governed by vertical heat extraction alone. Pavement heat storage, slope aspect and embankment geometry also redistribute heat laterally, creating uneven cooling across the road section [8,9,23,24]. Field observations and simulations link this uneven thermal field to uplifted 0 °C isotherms, convex permafrost tables and lateral temperature gradients [22,25]. These features can induce differential frost heave or thaw settlement [5,8,22]. In inclined TPCT embankments, they may concentrate tensile stress on the pavement and promote longitudinal cracking [22,26]. Thus, TPCT system design must consider not only ground cooling but also whether the cooling field is compatible with the cross-sectional thermal and deformation pattern of the embankment.

TPCT performance is controlled by both device-scale heat transfer and embankment-scale thermal regulation. Air temperature, boundary conditions, pipe geometry, inclination, burial depth and evaporator position control the operating period, heat-extraction depth and cooling range [16,18,19,27–30]. Semiconductor-assisted cooling has been explored to extend TPCT operation into the warm season, while lower ambient temperatures in high-latitude regions can increase cooling capacity without auxiliary refrigeration [31,32]. At the embankment scale, layout optimization has focused on reducing lateral thermal imbalance caused by slope aspect and pavement heat storage [8,9]. Bilateral TPCT arrangements provide more balanced cooling than unilateral, although sunny-shaded asymmetry persists [25,33]. L-shaped TPCTs and TPCT-insulation composite embankments extend cooling toward the embankment center and slope zones, but field evidence shows limited operating duration, persistent sunny-side warming and cracking when protection does not span the full cross-section [20,21,34]. Recent horizontal and self-adaptive horizontal TPCTs redistribute cooling along the embankment, reducing lateral temperature contrasts, smoothing isotherms and increasing heat release relative to inclined layouts [34–37]. Targeted arrays with variable-inclination evaporators have been used to cool localized warm zones in embankment–bridge transition sections by forming cold cores and raising the permafrost table [38]. These studies show that climate forcing, TPCT-scale design and embankment layout jointly control TPCT performance. For wide asphalt embankments, the unresolved issue is whether a layout can preserve laterally continuous frozen ground under asymmetric heat input [8,26,39]. Assessing this issue requires layout-level indicators, including lateral temperature uniformity, volumetric ice content, operating duration and cumulative cooling capacity.

This study evaluates how different TPCT layouts regulate the hydrothermal state of a wide asphalt embankment in a permafrost region under climate warming. A three-dimensional hydrothermal model is used to compare an embankment without TPCTs, a conventional inclined two-phase closed thermosyphon (CIT) layout and a base-arranged novel horizontal two-phase closed thermosyphon (NHT) layout. The analysis first characterizes degradation in the unprotected embankment and then examines how the two TPCT layouts affect temperature distribution, volumetric ice content, maximum thaw depth, operating duration and cumulative cooling capacity. By linking these indicators, this study assesses the ability of each layout to maintain frozen-state continuity and cross-sectional temperature uniformity, providing a basis for TPCT layout selection in wide asphalt embankments in permafrost regions.

2. Materials and Methods

Figure 2 summarizes the research workflow, including model inputs, hydrothermal model construction, initialization, validation, scenario simulation, indicator extraction and performance assessment. After natural ground validation, field monitoring data were used as indirect checks.

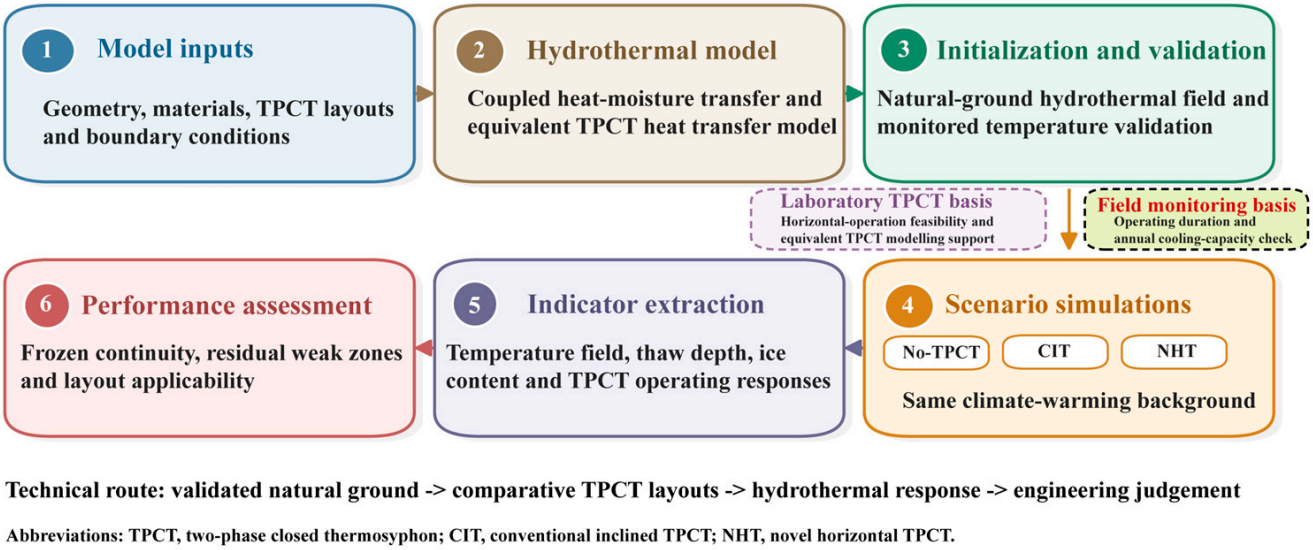


Figure 2. Research workflow.

2.1. Geometry

In the model coordinate system, x, y and z denote the transverse, longitudinal and vertical directions, respectively, and the natural ground surface is set at z = 0. Figure 3 shows the embankment cross-section, along-road computational unit and two TPCT layouts. The embankment has a 13 m crest width, a 3 m height and a side–slope ratio of 1:1.5. To reduce lateral boundary effects, the natural ground extends 39 m outward from both slope toes. The domain comprises embankment fill above the natural ground and three foundation layers: silty clay from 0 to 2 m, sub-clay from 2 to 8 m and weathered mudstone from 8 to 30 m. Layer-specific thermal and hydraulic parameters were assigned to represent differences in heat transfer, moisture migration and frozen-state evolution. A 0.1 m thick XPS insulation layer was placed 2 m above the embankment.

The CIT and NHT cases used identical pipe dimensions, evaporator and condenser lengths, condenser-fin parameters and computational-unit length but differed in evaporator orientation, installation position and cooling coverage. The CIT was inserted at 45° from below the XPS layer near the shoulder, whereas the NHT was placed horizontally along the embankment base. Both TPCTs had outer and inner diameters of 0.089 m and 0.08 m, a 10.5 m evaporator and a 2.5 m condenser. The condenser-fin height, thickness and spacing were 2.5 cm, 0.1 cm and 1 cm, respectively.

The 45° inclined TPCT was selected as a representative conventional layout used in previous engineering applications and laboratory studies [33,34]. This arrangement allows the evaporator to extend from the shoulder region toward the lower central part of the embankment and strengthen deep cooling beneath the embankment. Changing the inclination angle would alter evaporator burial depth, lateral coverage and cooling-field geometry. Therefore, this comparison is interpreted as a layout-level comparison rather than an optimization of inclination angle.

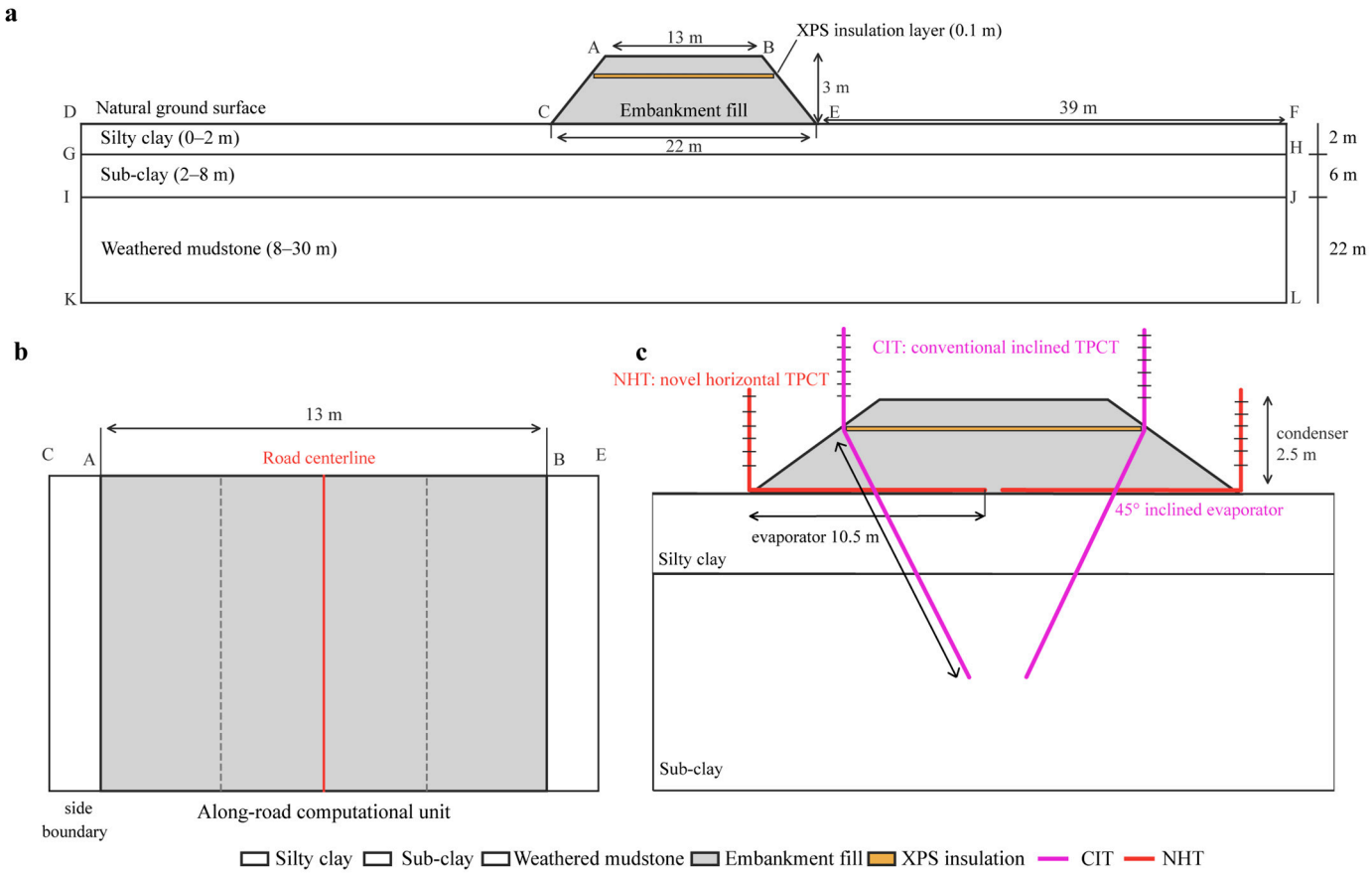


Figure 3. Physical model and TPCT layouts. (**a**) Embankment cross-section; (**b**) along-road computational unit; (**c**) CIT and NHT layouts.

2.2. Design Rationale and Experimental Basis of the NHT Layout

A laboratory-scale straight TPCT was tested experimentally to examine whether guided gas–liquid circulation could sustain heat transfer with a horizontal evaporator. The test system is shown in Figure 4a,b. Constant-temperature baths independently controlled the evaporator and condenser temperatures. Inside the TPCT, gas and liquid guide tubes separated vapor transport from condensate return (Figure 4c). A sealed separator was installed at the bottom of the condenser to maintain a liquid head and guide condensate return. The TPCT was tested at an inclination angle of 0° under different condenser-section temperatures. Each condition was repeated twice, and the heat flow rate was calculated from the stable 10 min average after steady heat transfer was reached. The TPCT maintained an effective heat flow rate at 0°, and the heat flow rate increased as the condenser-section temperature decreased (Figure 4d). The fitted correlations in Figure 4d were obtained from the mean values of the two repeated measurements at each condenser-section temperature. Compared with previously reported horizontal TPCTs that use wick structures, liquid collectors, and return lines for condensate redistribution, the present phase-separated design uses gas-guide and liquid-guide tubes together with a sealed separator to separate vapor transport from condensate return [34,36]. These data support horizontal operation and phase-separated circulation but were not used to calibrate the field-scale numerical model. The TPCT dimensions and test parameters are provided in Appendix A.

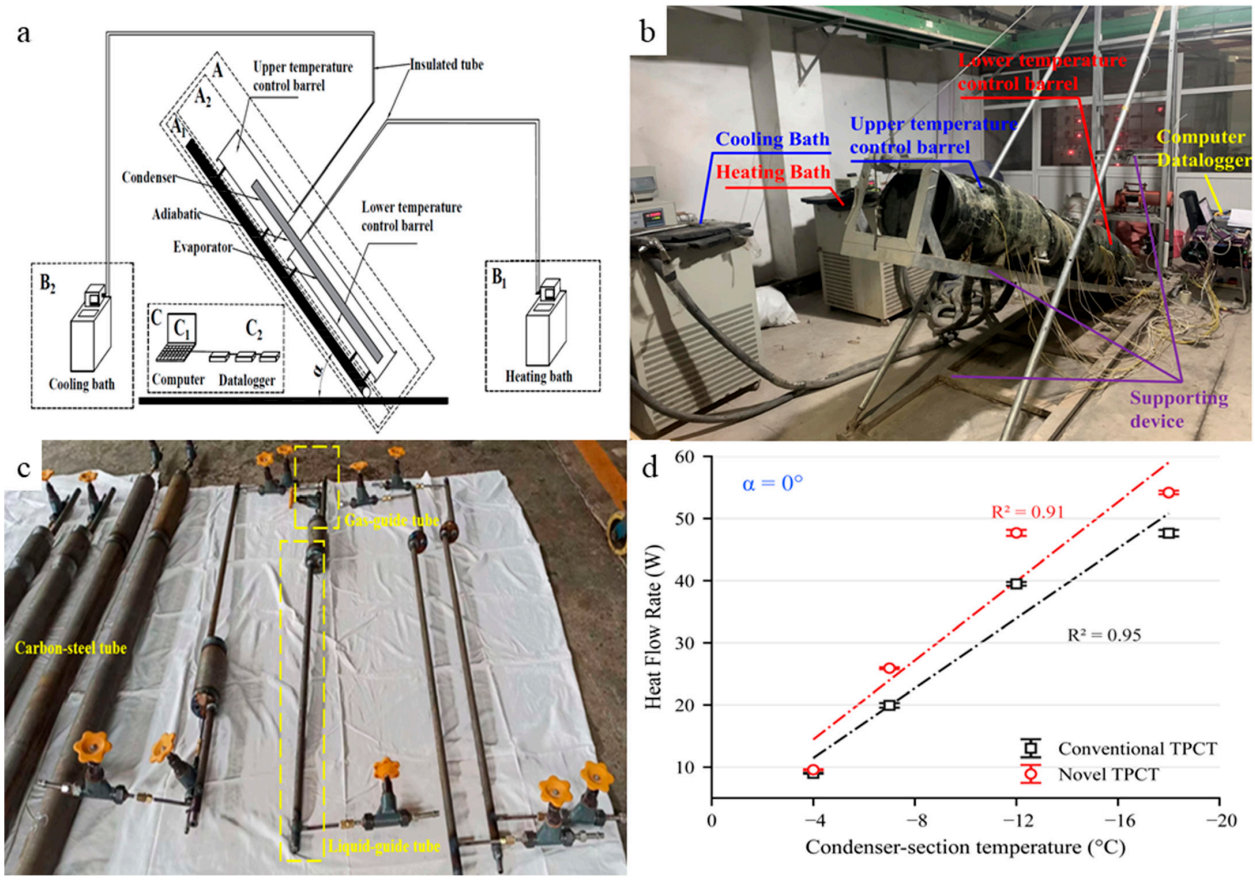


Figure 4. Experimental basis for horizontal TPCT operation. (**a**) Test system schematic; (**b**) physical view of the test system; (**c**) straight phase-separated TPCT; (**d**) heat flow rate at 0° under different condenser-section temperatures [28]. Error bars indicate standard deviations of two repeated measurements.

2.3. Governing Equations

In the hydrothermal model, temperature and unfrozen-water content were selected as the primary solution variables. Liquid-water migration was driven by unfrozen-water content gradients, temperature gradients and gravity, whereas ice was treated as immobile.

2.3.1. Coupled Hydrothermal Equations for Soil

Heat transfer in the soil–water–ice system was described as transient conduction with ice–water phase change. Based on energy conservation, the governing heat-transfer equation is expressed as [11,40]:

$$C_e \frac{\partial T}{\partial t} = \frac{\partial}{\partial x}\left(\lambda_e \frac{\partial T}{\partial x}\right) + \frac{\partial}{\partial y}\left(\lambda_e \frac{\partial T}{\partial y}\right) + \frac{\partial}{\partial z}\left(\lambda_e \frac{\partial T}{\partial z}\right) \quad (1)$$

where T is soil temperature (°C); t is time (s); x, y and z are spatial coordinates (m); C_e is the apparent equivalent volumetric heat capacity (J m^{-3} K^{-1}); and λ_e is the equivalent thermal conductivity (W m^{-1} K^{-1}).

Pore-water freezing and thawing were treated as continuous transitions over a finite phase-change interval. A smoothed step function was used to avoid abrupt changes in thermal properties near the freezing temperature:

$$H_f = H(\mathrm{T_f} - T, \Delta \mathrm{T}) \quad (2)$$

H is a smoothed function, T_f is the characteristic freezing temperature of the soil (°C), and ΔT is the phase-change smoothing interval (K), set to 0.5 K. H_f represents the local frozen-state fraction within the phase-change interval centered at T_f.

Soil thermal properties were updated according to the frozen-state fraction. In the apparent heat-capacity method, the equivalent volumetric heat capacity includes sensible heat storage and latent heat release. The equivalent thermal conductivity includes conductive heat transfer and latent-heat redistribution associated with unfrozen-water migration [4,33]:

$$C_e = C_u\rho_s(1 - H_f) + C_f\rho_s H_f + L\rho_w\frac{\partial\theta_u}{\partial T} \tag{3}$$

$$\lambda_e = \lambda_u(1 - H_f) + \lambda_f H_f + L\rho_w D_w\frac{\partial\theta_u}{\partial T} \tag{4}$$

where C_u and C_f are the specific heat capacities of thawed and frozen soil, respectively (J kg^{-1} K^{-1}); ρ_s is the dry density (kg m^{-3}); L is the latent heat of ice–water phase change (J kg^{-1}); ρ_w is the density of water (kg m^{-3}); λ_u and λ_f are the thermal conductivities of thawed and frozen soil, respectively (W m^{-1} K^{-1}); D_w represents moisture diffusion associated with the unfrozen-water content gradient (m^2 s^{-1}); and θ_u is the unfrozen-water content (m^3 m^{-3}).

In frozen soil, only liquid unfrozen water was assumed to migrate, whereas ice remained immobile. The moisture mass-conservation equation is written as [11,33]:

$$\frac{\partial\theta_u}{\partial t} + \frac{\rho_i}{\rho_w}\frac{\partial\theta_i}{\partial t} = -\left(\frac{\partial q_{wx}}{\partial x} + \frac{\partial q_{wy}}{\partial y} + \frac{\partial q_{wz}}{\partial z}\right) \tag{5}$$

where θ_i is the volumetric ice content (m^3 m^{-3}); ρ_i and ρ_w are the densities of ice and water, respectively (kg m^{-3}); and q_{wx}, q_{wy} and q_{wz} are the liquid-water flux components in the x, y and z directions, respectively (m s^{-1}).

Liquid-water flux was driven by gradients in unfrozen-water content and temperature, with gravity included in the vertical direction:

$$\begin{aligned} q_{wx} &= -\left(D_w\frac{\partial\theta_u}{\partial x} + D_T\frac{\partial T}{\partial x}\right) \\ q_{wy} &= -\left(D_w\frac{\partial\theta_u}{\partial y} + D_T\frac{\partial T}{\partial y}\right) \\ q_{wz} &= -\left(D_w\frac{\partial\theta_u}{\partial z} + D_T\frac{\partial T}{\partial z} + K_w\right) \end{aligned} \tag{6}$$

where D_T represents temperature-gradient-driven moisture diffusion, and K_w is the hydraulic conductivity (m s^{-1}). The units of D_w and D_T are m^2 s^{-1} and m^2 s^{-1} K^{-1}, respectively.

Under frozen conditions, adsorption on soil-particle surfaces and physicochemical effects retain part of the pore water in an unfrozen state. The temperature-dependent unfrozen-water content was described by an empirical relation [41]:

$$\theta_u = H_f(a_1|T - T_f|^{-b_1} + \theta_r) + (1 - H_f)\theta_{tot} \tag{7}$$

where θ_r is the residual volumetric water content (m^3 m^{-3}), θ_{tot} is the total volumetric water content (m^3 m^{-3}), and a_1 and b_1 are empirical parameters for the unfrozen-water characteristic curve.

During freezing, ice formation reduces liquid-water pathways and decreases hydraulic conductivity and moisture diffusivity. The freezing-impedance effect was described by empirical functions of volumetric ice content [33,42,43]:

$$K_w = \frac{a_2\theta_u^{b_2}}{10^{10\theta_i}} \tag{8}$$

$$D_w = \frac{a_3 \theta_u^{b_3}}{10^{10\theta_i}} \tag{9}$$

where a_2 and a_3 are empirical coefficients for hydraulic conductivity and water diffusivity, respectively.

Equations (1)–(9) constitute the hydrothermal model for the soil domain. Temperature controls ice–water phase transformation and the associated thermal and moisture-migration parameters. Unfrozen-water migration and phase change update the unfrozen-water content, freezing state and latent-heat effects. All symbols and physical meanings are summarized in Appendix C.

2.3.2. Equivalent Heat-Transfer Model for TPCTs

To avoid numerical instability caused by resolving internal two-phase flow in long-term embankment-scale simulations, TPCT heat transfer was represented by an equivalent thermal-resistance method. Because the condenser was not explicitly resolved in the model, the equivalent resistance was treated as a lumped system resistance that includes pipe-wall conduction, internal phase-change heat transfer and condenser-air heat exchange. The same equivalent-resistance framework was used for the CIT and NHT cases to isolate layout-scale effects related to evaporator position and cooling coverage. The cooling effect was applied as an equivalent heat-absorption flux at the evaporator boundary:

$$-\lambda_e \nabla T \cdot n_{TPCT} = q_{TPCT} \tag{10}$$

where λ_e is the equivalent thermal conductivity of soil (W m^{-1} K^{-1}), n_{TPCT} is the outward normal of the evaporator boundary, and q_{TPCT} is the equivalent heat flux absorbed from the soil by the evaporator segment (W m^{-2}).

TPCT operation was controlled by the effective temperature difference between the evaporator and ambient air. A smooth activation function was used to represent start-up and shut-down:

$$S_{on} = H(T_{evap} - T_{air} - \Delta T_{start}, \Delta T_{on}) \tag{11}$$

where S_{on} is the TPCT activation factor; T_{evap} is the mean wall temperature of the evaporator (°C); T_{air} is the ambient air temperature (°C); ΔT_{start} is the TPCT start-up temperature difference (K), set to 1 K; and ΔT_{on} is the start-up smoothing interval (K).

The heat-transfer power of a single TPCT was calculated from the effective evaporator-air temperature difference and the equivalent total thermal resistance. It was then converted into an equivalent heat-absorption flux on the evaporator boundary [28–30]:

$$q_{TPCT} = \frac{Q_{TPCT}}{A_{eo}} = S_{on} \frac{T_{evap} - T_{air} - \triangle T_{start}}{A_{eo} R_{TPCT}} \tag{12}$$

where Q_{TPCT} is the heat-transfer power of TPCT (W), A_{eo} is the outer heat-exchange area of the evaporator (m^2), R_{TPCT} is the equivalent total thermal resistance (K W^{-1}), and q_{TPCT} is the equivalent evaporator heat flux (W m^{-2}).

The equivalent total thermal resistance was decomposed into pipe-wall conduction, internal phase-change heat transfer and condenser-side air convection:

$$R_{TPCT} = R_{ew} + R_{ei} + R_{ci} + R_{cw} + R_{co} \tag{13}$$

where R_{ew} and R_{cw} are the wall conduction resistances of the evaporator and condenser, respectively; R_{ei} and R_{ci} are the phase-change resistances in evaporator and condenser, respectively; and R_{co} is the convective resistance between the condenser outer surface and ambient air. All resistance terms have units of K W^{-1}.

The individual thermal-resistance components can be expressed as:

$$\begin{aligned} R_{ew} &= \frac{1}{2\pi\lambda_{TPCT}L_e}\ln\left(\frac{d_o}{d_i}\right) \\ R_{ei} &= \frac{1}{A_e\alpha_e} \\ R_{ci} &= \frac{1}{A_c\alpha_c} \\ R_{cw} &= \frac{1}{2\pi\lambda_{TPCT}L_c}\ln\left(\frac{d_o}{d_i}\right) \\ R_{co} &= \frac{1}{A_f\alpha_a} \end{aligned} \quad (14)$$

where λ_{TPCT} is the thermal conductivity of the pipe wall (W m^{-1} K^{-1}); L_e and L_c are the evaporator and condenser lengths, respectively (m); d_o and d_i are the outer and inner pipe diameters, respectively (m); α_e, α_c and α_a are the evaporator-side boiling, condenser-side condensation and condenser-air convective heat-transfer coefficients, respectively (W m^{-2} K^{-1}); and A_e, A_c and A_f are the corresponding evaporator inner, condenser inner and finned condenser outer heat-exchange areas, respectively (m^2).

Equations (10)–(14) couple the TPCT with the soil temperature field. This formulation supports layout-level comparison but does not resolve inclination-dependent internal two-phase-flow resistance. It also excludes long-term device ageing, including environmental corrosion, non-condensable gas formation and leakage caused by external damage, which may influence field-scale thermal resistance during multi-decade service.

2.4. Boundary Conditions and Material Parameters

Solar radiation, wind speed, air temperature and surface materials impose different thermal conditions on the natural ground, embankment slopes and asphalt pavement. Equivalent surface-temperature boundaries were prescribed to represent these periodic surface-temperature variations [20,33,44]:

$$T_s = \mathrm{T}_0 + \mathrm{A}\cdot\sin\left(\frac{2\pi t}{8760} + \varphi\right) + \frac{\Delta T_{\mathrm{air}}}{8760}\cdot t \quad (15)$$

where T_s is the equivalent surface temperature (°C), T_0 is the annual mean surface temperature (°C), A is the annual temperature amplitude (°C), and φ is the initial phase (rad). ΔT_{air} is the prescribed climate-warming rate for the study region (°C yr^{-1}), set to 0.052 °C yr^{-1}.

Equivalent surface-temperature boundaries were used to represent surface-material, slope-aspect and regional-warming effects. Asphalt pavement was assigned a higher annual mean surface temperature than natural ground, and the sunny slope a higher value than the shaded slope. The parameters in Table 1 were derived from Beiluhe station monitoring data and previous Qinghai–Tibet Plateau embankment studies [25,33,34], with annual mean temperature and amplitude integrating air temperature, radiation, wind-driven convection and surface properties. The warming rate of 0.052 °C yr^{-1} was applied as a regional high-altitude permafrost-corridor scenario for three cases [45]. The south-facing and north-facing slopes represent the traditional sunny-shaded contrast for an east–west road in the Northern Hemisphere; other orientations can be assessed by interpolating or recalculating equivalent surface-temperature parameters according to slope azimuth and local radiation-meteorological conditions.

The lateral boundaries (DK-FL) were set as zero normal-flux boundaries, and an upward geothermal heat flux of 0.03 W m^{-2} was applied at the bottom boundary (KL). The XPS insulation layer was excluded from the moisture-field calculation. Parameters in Tables 2 and 3 were obtained from field investigation, laboratory tests and hydrothermal parameters for the study region [25,33,34]. The water, ice and residual-water contents are expressed as relative volumetric contents (m^3 m^{-3}).

Table 1. Temperature parameters for different boundaries.

Location	Annual Mean Temperature/°C	Annual Temperature Amplitude/°C
Natural ground surface	−0.5	9.2
Sunny slope	3.3	10.6
Shaded slope	0.5	12
Asphalt pavement	4.1	14

Table 2. Basic physical and thermal parameters of soils.

Parameter	Embankment Fill	Silty Clay	Sub-Clay	Weathered Mudstone	XPS	Unit
θ_r	0.02	0.05	0.05	0.05		$m^3\ m^{-3}$
n	0.25	0.3	0.4	0.2		$m^3\ m^{-3}$
S	0.85	0.8	0.85	0.8		dimensionless
ρ_s	2050	1930	1890	2000	40	$kg\ m^{-3}$
λ_u	1.629	1.55	1.124	1.474	0.03	$W\ m^{-1}\ K^{-1}$
λ_f	1.98	1.751	1.351	1.824		$W\ m^{-1}\ K^{-1}$
C_u	1173.5	1241	1227	1049.5	1400	$J\ kg^{-1}\ K^{-1}$
C_f	996	889	1078.6	923		$J\ kg^{-1}\ K^{-1}$

Table 3. Empirical parameters for moisture migration and permeability.

Parameter	Embankment Fill	Silty Clay	Sub-Clay	Weathered Mudstone	Unit
a_1	0.073	0.141	0.102	0.025	Dimensionless
b_1	0.497	0.32	0.242	0.581	Dimensionless
a_2	5.88×10^{-5}	2×10^{-5}	1.5×10^{-5}	2.55×10^{-6}	$m\ s^{-1}$
b_2	16.4	14.59	11.27	5.57	Dimensionless
a_3	1.4×10^{-6}	4.7×10^{-6}	1.52×10^{-6}	2.17×10^{-7}	$m^2\ s^{-1}$
b_3	3.98	7.18	4.45	1.95	Dimensionless
χ_T	0.05	0.08	0.08	0.05	Dimensionless

Before embankment construction, the natural ground was simulated without climate warming until a quasi-steady hydrothermal state was obtained. This state provided the initial temperature and moisture fields for the soil domain. The embankment fill was initialized from its initial saturation and surface thermal condition. Climate-warming surface-temperature boundaries were then applied to three cases.

Local mesh refinement was applied in the TPCT–soil contact zone, embankment and shallow foundation. The maximum element size was 0.1 m at the TPCT–soil contact boundary, 0.25 m in the embankment region, 0.1 m in the silty clay layer and 0.15 m in the sub-clay layer. The weathered mudstone layer used a graded mesh with a maximum element size of 1 m and a growth ratio of 3. Quadratic Lagrange elements were adopted, and the final model contained approximately 5.36×10^5 degrees of freedom. The transient solver used a maximum time step of 1 d and a relative tolerance of 1×10^{-4}.

Model reliability was checked using natural ground validation, mesh sensitivity and time-step sensitivity. The quasi-steady natural ground temperature profile was compared with field observations. Mesh refinement produced a maximum-thaw-depth difference of 0.04 m at the sunny-side slope toe. The 1 d and 0.1 d maximum time steps produced small differences in TPCT heat-flux-density response, with maximum deviations of 0.96 $W\ m^{-2}$ on the sunny side and 1.10 $W\ m^{-2}$ on the shaded side. The laboratory horizontal-TPCT test supported the feasibility of NHT operation, but was not used to validate the embankment-scale cooling simulation.

3. Results and Discussion

3.1. Baseline Hydrothermal Field and Model Validation for the Natural Ground

The quasi-steady natural ground during the maximum thaw period was used as the baseline hydrothermal field and validation benchmark before embankment construction. Figure 5a shows a vertically stratified temperature field with limited lateral variation, reflecting the prescribed surface-temperature boundary and layer-dependent thermal properties. The 0 °C isotherm was located at about 2 m depth, consistent with the natural maximum thaw depth. The simulated temperature profile agreed with field observations, with a mean absolute error of 0.11 °C, a root-mean-square error of 0.18 °C and an R^2 of 0.95 (Figure 5b). The simulated and monitored 0 °C isotherm depths differed by 0.08 m.

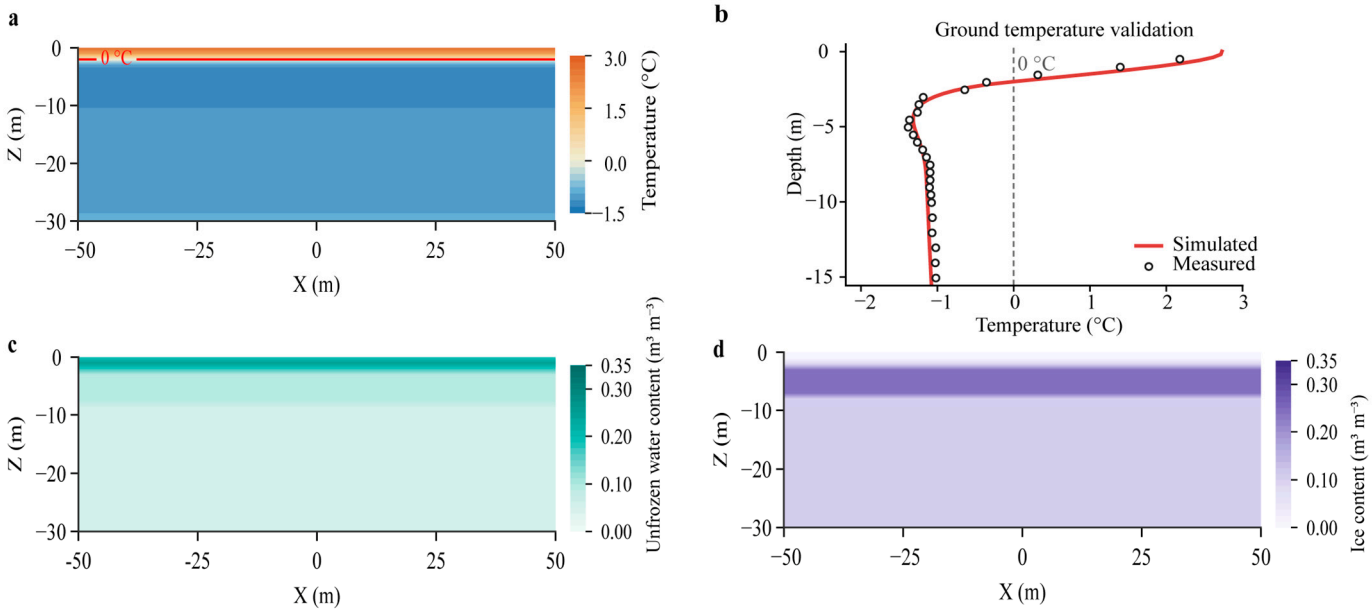


Figure 5. Quasi-steady hydrothermal field and validation of the natural ground. (**a**) Temperature field; (**b**) temperature-profile validation; (**c**) relative total volumetric water content (m^3 m^{-3}); (**d**) relative volumetric ice content (m^3 m^{-3}).

Figure 5c,d show the relative total volumetric water content and relative volumetric ice content. Total water content was governed primarily by layer-specific porosity and initial saturation, with minor within-layer variations caused by freeze-thaw water redistribution. Volumetric ice content varied with both temperature and total water content. During the maximum thaw period, high ice content remained in the permafrost layer, and the sub-clay layer formed the main high-ice-content zone. Weathered mudstone contained less ice owing to lower porosity and limited water storage.

3.2. Hydrothermal Degradation of the No-TPCT Reference Embankment Under Warming

3.2.1. Spatial Degradation Pattern During the Maximum Thaw Period

The no-TPCT reference case was used to identify the degradation pattern that required thermal control. Permafrost degradation beneath the embankment was asymmetric, with deep thaw concentrated below the embankment center and thermal disturbance extending toward the sunny side (Figure 6a,b). Heat stored in the asphalt pavement and embankment fill promoted downward heat transfer beneath the centerline. Stronger solar radiation on the sunny slope increased shallow warm-season heat input and drove lateral thermal erosion toward the sunny-side slope toe. The weaker disturbance at the shaded-side slope toe indicates that slope aspect and embankment width jointly controlled the asymmetric degradation pattern [7,8].

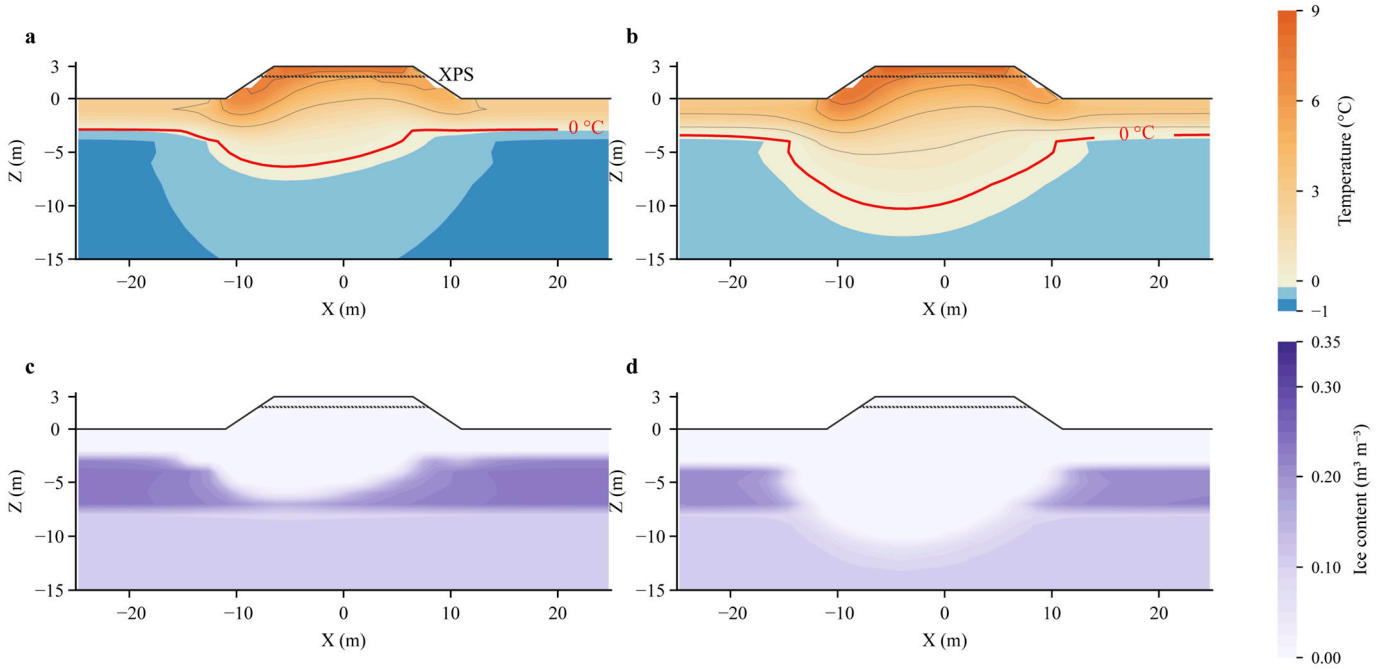


Figure 6. Hydrothermal fields of the no-TPCT reference embankment during the maximum thaw period in years 10 and 20. (**a**) Temperature field in year 10; (**b**) temperature field in year 20; (**c**) relative volumetric ice content (m^3 m^{-3}) in year 10; (**d**) relative volumetric ice content (m^3 m^{-3}) in year 20.

The ice-content field evolved consistently with the temperature field and highlighted the loss of frozen-state continuity (Figure 6c,d). In year 10, the low-ice-content zone was mainly confined beneath the embankment body and shoulders, indicating early disturbance of the shallow frozen state. By year 20, this zone had expanded downward and toward the sunny side, cutting through the original high-ice-content band in the sub-clay layer. These changes show reduced frozen-water storage and a weakened frozen foundation zone beneath the wide embankment.

3.2.2. Quantitative Thaw-Depth Evolution at Representative Locations

Ground-temperature profiles and maximum thaw depths at representative transverse locations quantified the non-uniform degradation pattern (Figure 7 and Table 4). In Figure 7, Year 1, Year 5, Year 10, Year 15 and Year 20 denote the time after embankment construction. The 0 °C isotherm moved downward at all locations, but the magnitude varied across the cross-section. By year 20, the maximum thaw depth reached 9.76 m beneath the embankment center and 10.06 m at the sunny-side shoulder. The cumulative increases at these two locations were 8.03 and 7.99 m, respectively, showing strong downward heat transfer beneath the embankment body and sunny-side shoulder. In contrast, the shaded-side slope toe increased by only 1.49 m and remained outside the main disturbed zone. This contrast confirms that degradation of the wide asphalt embankment must be evaluated across the full cross-section.

Table 4. Maximum thaw depth at representative locations of the no-TPCT embankment.

Location	Year 1/m	Year 20/m	Cumulative Increase/m	Degradation Feature
Sunny slope toe	2.45	8.3	5.85	Thermal disturbance expands toward the outer slope toe
Sunny shoulder	2.07	10.06	7.99	Strongly degraded sunny-side zone

Table 4. *Cont.*

Location	Year 1/m	Year 20/m	Cumulative Increase/m	Degradation Feature
Embankment center	1.73	9.76	8.03	Dominant deep-thaw zone
Shaded shoulder	2.04	7.14	5.1	Moderate degradation
Shaded slope toe	2.43	3.92	1.49	Weak-response zone

Maximum thaw depth is positive downward from the natural ground surface.

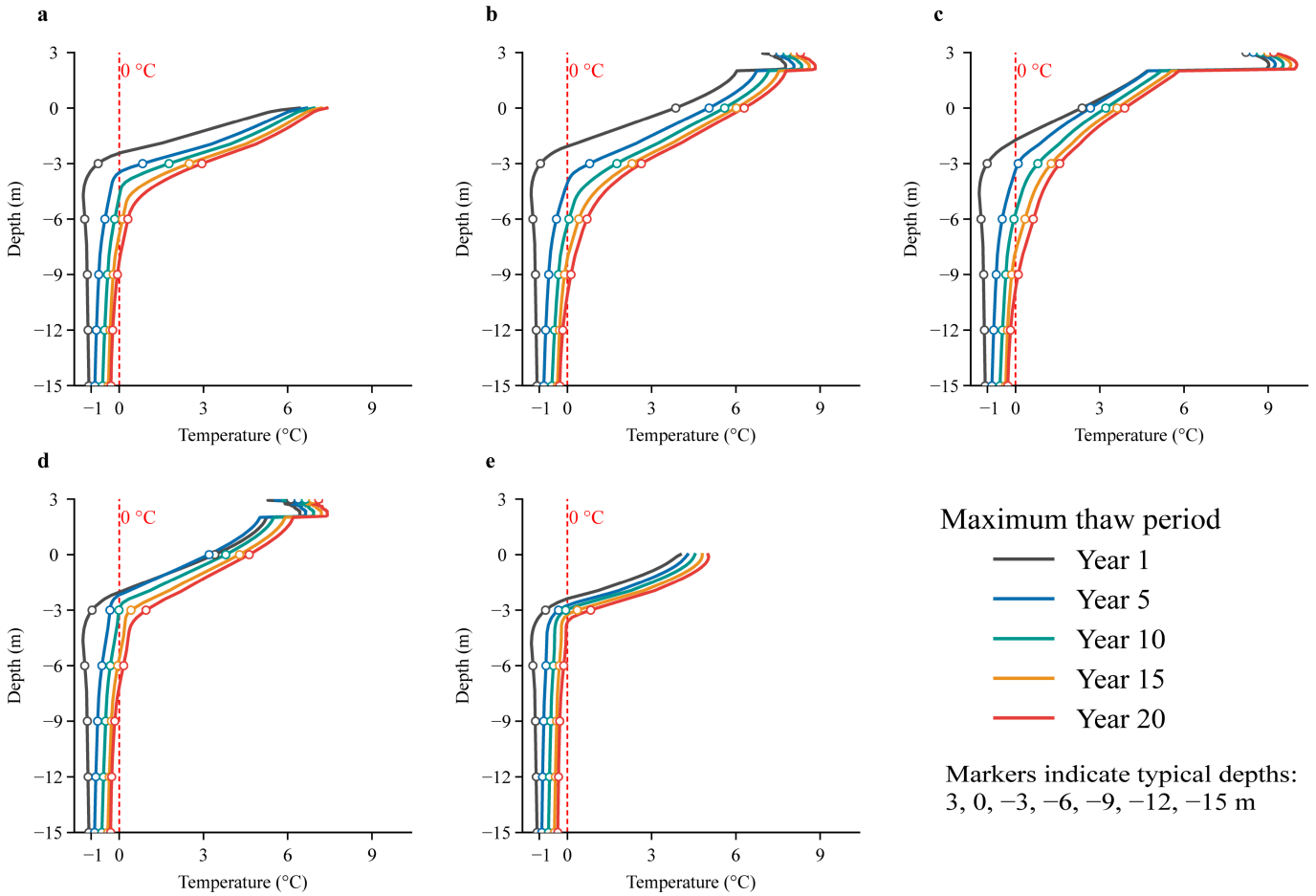


Figure 7. Ground-temperature profiles at representative locations of the no-TPCT reference embankment during the maximum thaw period. (**a**) Sunny-side slope toe; (**b**) sunny-side shoulder; (**c**) embankment center; (**d**) shaded-side slope toe; (**e**) shaded-side shoulder.

Temporal thaw-rate increments show that degradation varied by both location and stage (Figure 8). The embankment center and sunny-side shoulder had the highest mean rates over years 1–20, reaching 0.423 and 0.420 m yr^{-1}, respectively. Both locations increased rapidly during the early stage, consistent with strong downward thermal disturbance beneath the embankment body and sunny-side shoulder. At the sunny-side slope toe, the thaw-rate increment increased during years 10–15 and reached 0.413 m yr^{-1}. This delayed peak indicates lateral expansion of thermal disturbance toward the outer sunny-side toe. The shaded-side slope toe showed only a weak response, with a mean rate of 0.067 m yr^{-1}. The shaded-side shoulder showed a delayed peak during years 10–15, indicating an intermediate response between the embankment body and the shaded-side toe.

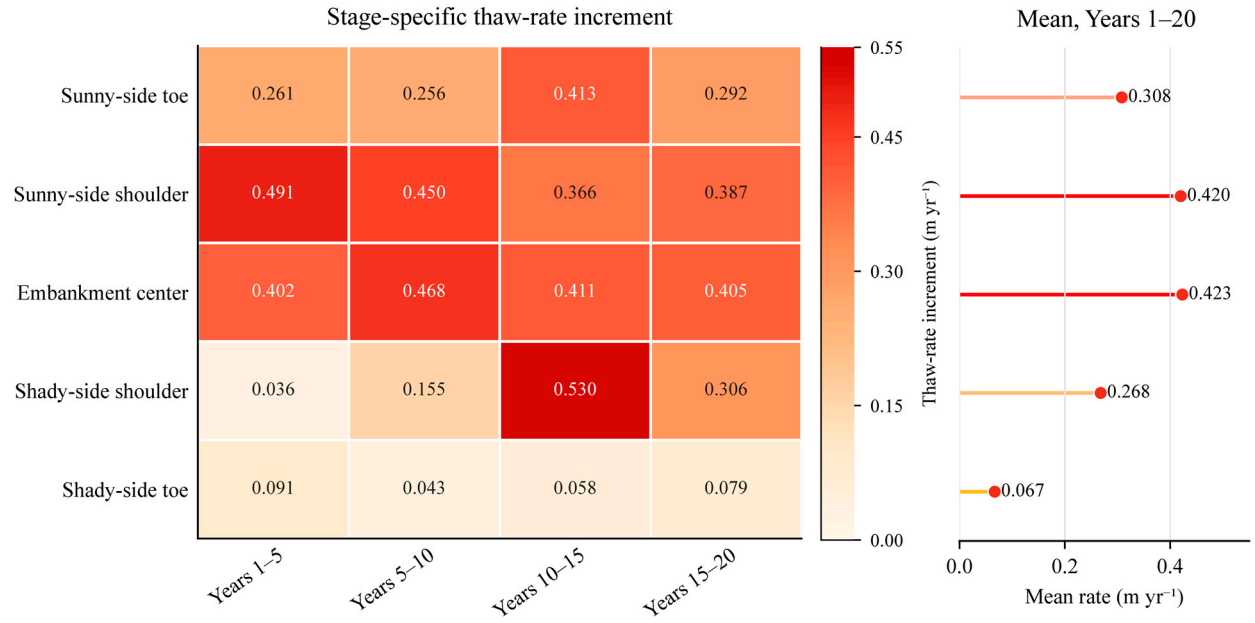


Figure 8. Average growth rate of maximum thaw depth at representative locations of the no-TPCT reference embankment during different stages.

3.3. Hydrothermal Regulation by CIT and NHT Measures During Representative Periods

3.3.1. Temperature-Field Regulation During the Maximum Thaw Period

Figure 9 compares the maximum-thaw-period temperature fields of the CIT and NHT embankments. Compared with the no-TPCT case, both layouts suppressed the downward migration of the 0 °C isotherm, but they produced different cooling geometries. In the CIT case, the inclined evaporators concentrated cooling in the deeper soil beneath the embankment. A deep low-temperature core formed near the evaporator influence zone, reducing vertical heat penetration below the embankment center [22,25,33]. Cooling weakened toward the outer shoulder, shallow side slope and slope toe, where the temperature field remained near the edge of the TPCT influence range.

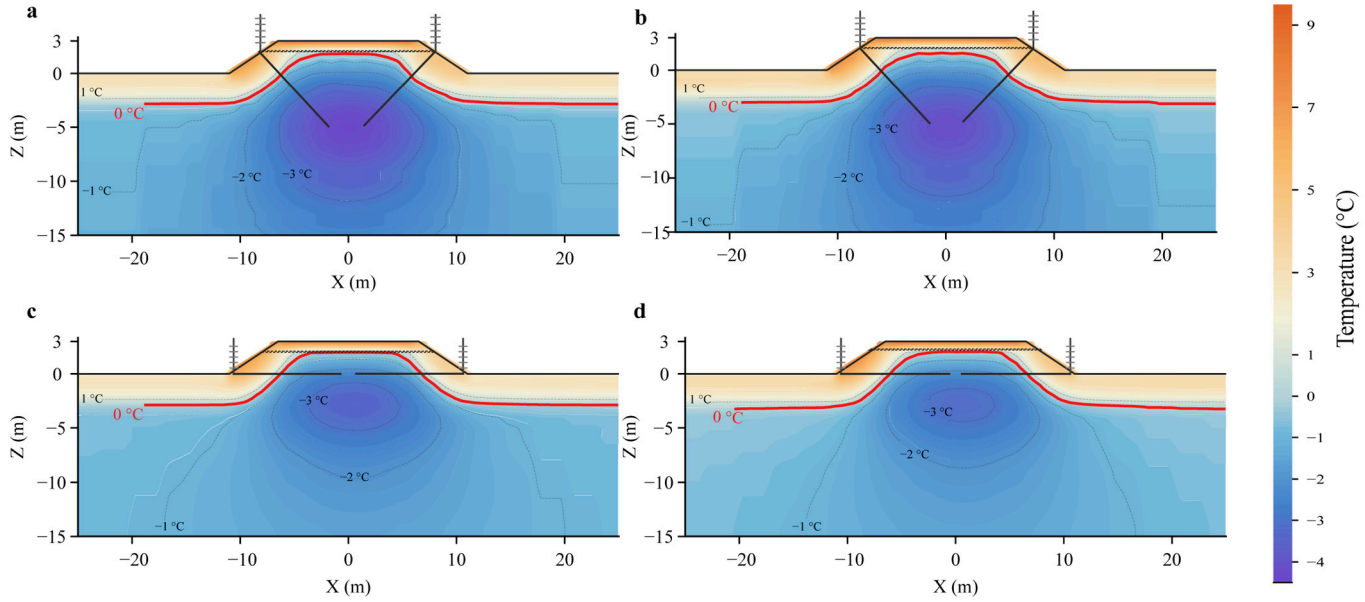


Figure 9. Comparison of maximum-thaw-period temperature fields between the CIT and NHT embankments. (**a**) Year 10-CIT; (**b**) Year 20-CIT; (**c**) Year 10-NHT; (**d**) Year 20-NHT.

In the NHT case, the horizontal evaporator was placed along the embankment base, close to the shallow zone affected by pavement and embankment heat storage. This arrangement formed a laterally continuous shallow subzero belt and extended the −1 °C and −2 °C isotherms toward both sides of the embankment. The main effect of the NHT was not to produce the lowest local temperature, but to redistribute cooling along the basal heat-entry zone [34,36]. Compared with the CIT layout, this improved shallow frozen-state continuity and cross-sectional temperature uniformity.

3.3.2. Ice-Content Continuity and Thaw-Depth Response

The layout-dependent difference in frozen-state evolution was already visible after the first cold season (Figure 10). In the CIT case, relative volumetric ice content increased locally around the inclined evaporator influence zone, but low-ice-content areas remained within the embankment body and near the embankment base. Shallow lateral freezing was therefore still discontinuous during the initial operating stage. In the NHT case, the horizontal evaporator formed a more continuous frozen belt along the embankment base and reduced the low-ice-content area beneath the centerline. This early response indicates that the horizontal layout improved shallow frozen-state continuity from the beginning of TPCT operation.

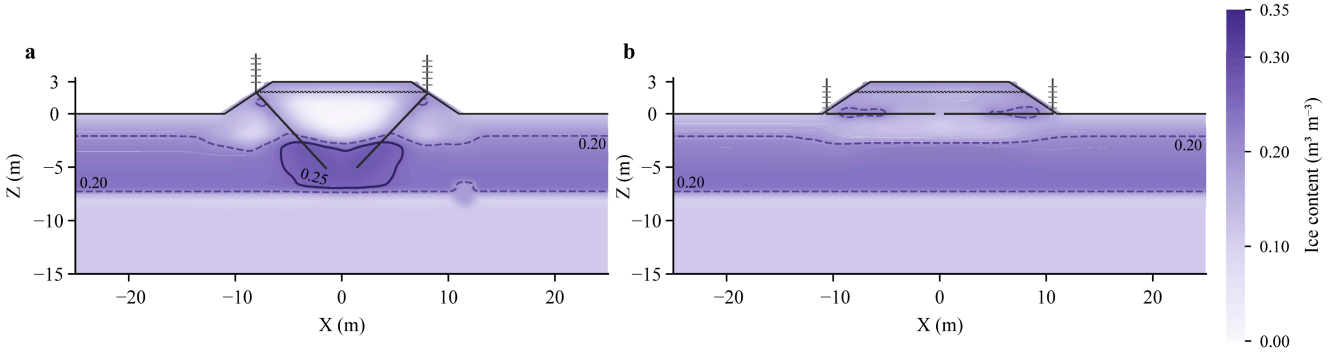


Figure 10. Relative volumetric ice-content distribution (m^3 m^{-3}) at the end of the first cold season. (**a**) CIT; (**b**) NHT.

During the maximum thaw period in year 20, both TPCT layouts reduced frozen-water loss beneath the embankment, but they produced different relative volumetric ice-content structures (Figure 11). The CIT case showed larger lateral variation near the shoulders and slope toes, indicating persistent discontinuity between the TPCT-affected zone and the outer embankment zones. The NHT case beneath the embankment body was more laterally connected, with no clear low-ice-content break across the basal frozen zone. The transverse profile in Figure 11c quantifies this difference. The lateral range of relative volumetric ice content, defined as the maximum minus the minimum value, was 0.103 m^3 m^{-3} for the CIT layout and 0.054 m^3 m^{-3} for the NHT layout. The smaller range indicates that the NHT reduced cross-sectional ice-content variability mainly by improving shallow frozen-state continuity, rather than by forming a deep localized cooling core.

Ground-temperature profiles and 0 °C isotherm depths quantified the layout-dependent cooling differences (Figure 12 and Table 5). Under TPCT cooling, the continuous downward migration seen in the no-TPCT case changed to upward migration or near stability at the embankment center and shoulders. Maximum thaw depth is reported as positive downward from the natural ground surface. Negative values indicate that the 0 °C isotherm lies above the z = 0 reference level during the maximum thaw period. At the embankment center, the year-20 value changed from 9.76 m in the no-TPCT case to −1.61 m under the CIT and −2.00 m under the NHT. At the sunny-side shoulder, it changed from

10.06 m to 0.53 m and 0.48 m, respectively. By contrast, the sunny-side slope toe still had year-20 thaw depths of 2.94 m under the CIT and 3.03 m under the NHT. In both protected cases, the sunny-side slope toe remained more thermally disturbed than the shaded-side toe, indicating that toe-focused protection or layout optimization remains necessary.

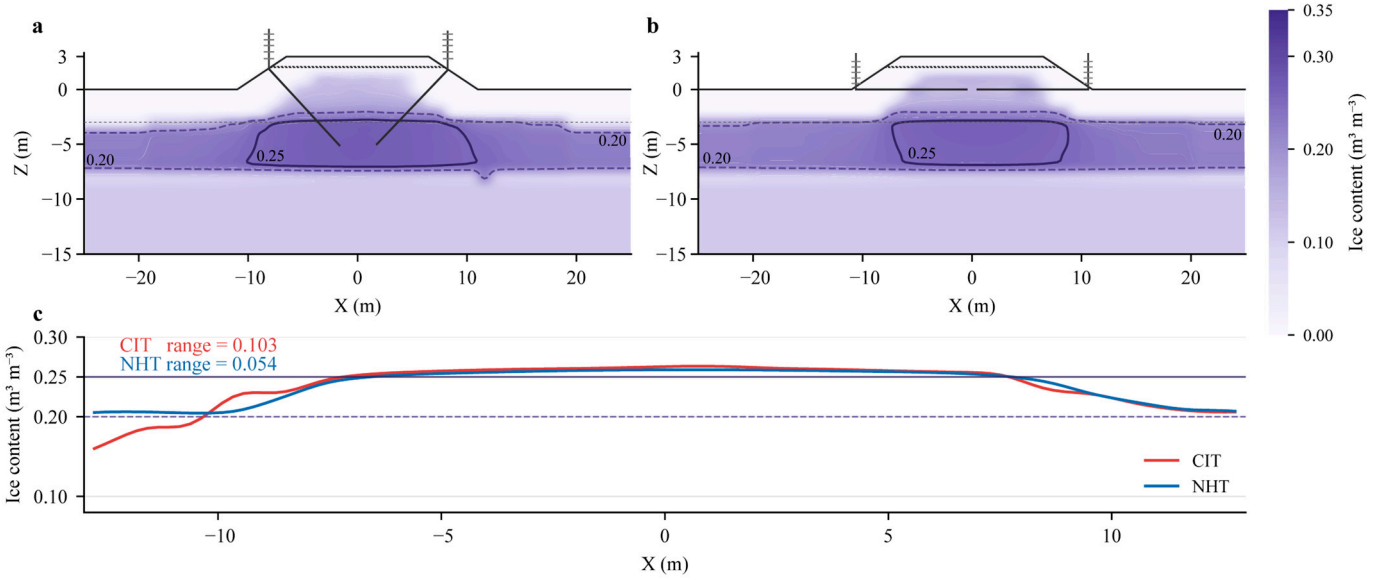


Figure 11. Relative volumetric ice-content distribution (m^3 m^{-3}) during the maximum thaw period in year 20. (**a**) CIT; (**b**) NHT; (**c**) transverse ice-content profiles.

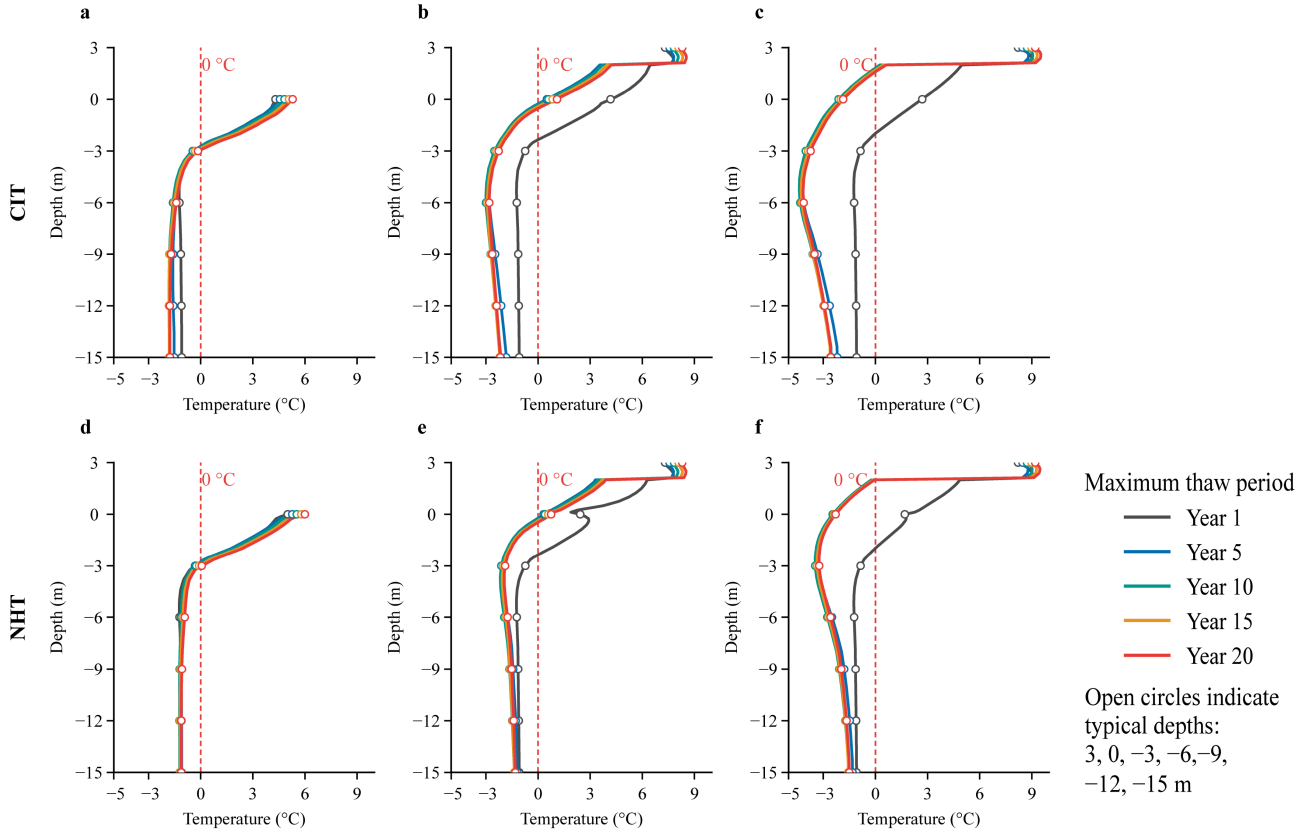


Figure 12. Ground-temperature profiles during the maximum thaw period. (**a**–**c**) CIT layout at the sunny-side slope toe, sunny-side shoulder and embankment center; (**d**–**f**) NHT layout at the same locations.

Table 5. Maximum thaw depth at representative locations under different TPCT measures.

Location	CIT			NHT		
	Year 1/m	Year 20/m	Change/m	Year 1/m	Year 20/m	Change/m
Sunny slope toe	2.8	2.94	0.14	2.79	3.03	0.24
Sunny shoulder	2.35	0.53	−1.82	2.35	0.48	−1.87
Embankment center	1.98	−1.61	−3.59	1.96	−2	−3.96
Shaded shoulder	2.45	0.96	−1.49	2.4	−0.14	−2.54
Shaded slope toe	2.7	2.66	−0.04	2.71	2.61	−0.1

Maximum thaw depth is positive downward from the natural ground surface. The change is the difference between year 20 and year 1, and negative values indicate upward movement.

The time–depth temperature evolution at the slope toes shows the persistence of lateral thermal disturbance after embankment construction and TPCT cooling (Figure 13). In the no-TPCT case, the 0 °C isotherm at the sunny-side slope toe moved progressively downward over 20 years, indicating delayed lateral heat propagation from the embankment body toward the outer toe. The shaded-side slope toe also experienced seasonal freeze-thaw oscillations, but its long-term 0 °C isotherm migration was weaker. This contrast indicates that slope aspect controlled the lateral thermal disturbance.

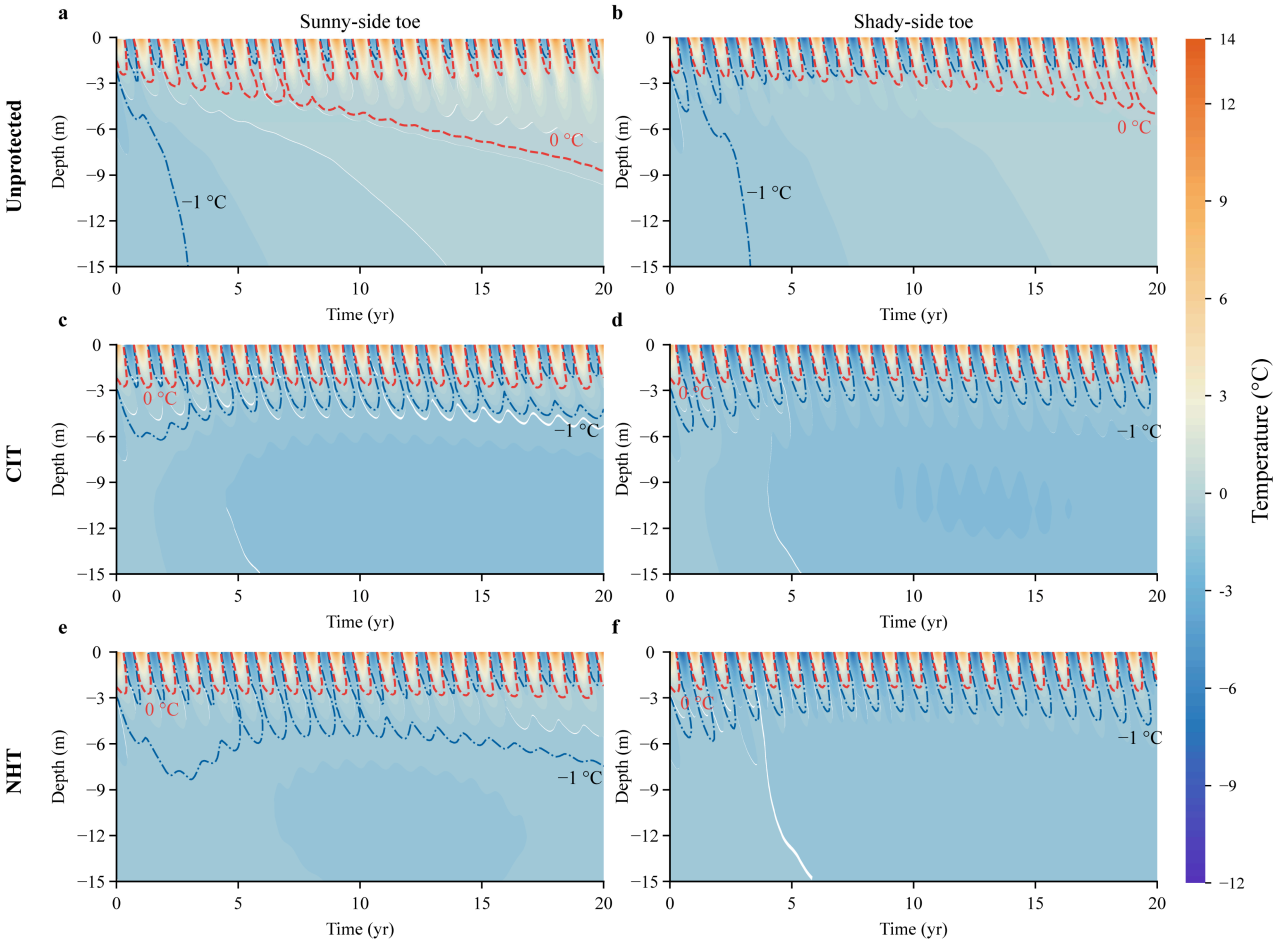


Figure 13. Time–depth temperature evolution at both slope toes. (**a**,**c**,**e**) Sunny-side slope toe; (**b**,**d**,**f**) shaded-side slope toe.

Both TPCT layouts limited the downward migration of the 0 °C isotherm at the slope toes, but neither removed the sunny-shaded difference. Under the CIT layout, the −1 °C isotherm remained more stable at greater depth, reflecting stronger deep cooling from the

inclined evaporator. Under the NHT layout, cooling was concentrated along the shallow basal zone, and the −1 °C isotherm still differed between the sunny and shaded toes. This difference remained within the subzero field and did not develop into a persistent downward migration of the 0 °C isotherm. The NHT therefore maintained the frozen state at the slope toes mainly through shallow basal cooling, whereas the CIT provided stronger deep local control. In both protected cases, the sunny-side slope toe remained more thermally disturbed than the shaded-side toe, making it the main residual weak zone for layout optimization.

3.4. Explanation Based on Equivalent TPCT Operating Responses

The different hydrothermal effects of the two layouts were associated with their TPCT operating responses (Figure 14). Both layouts showed seasonal start-up and shut-down. Heat flux density increased rapidly after the onset of cold-season cooling, reached a peak in mid-cold season and decreased to nearly zero during the warm season [17,25,27]. The first operating years had higher peaks because warmer post-construction soil increased the evaporator-air temperature difference. As the soil around the evaporator cooled, the operating response decreased and became more stable.

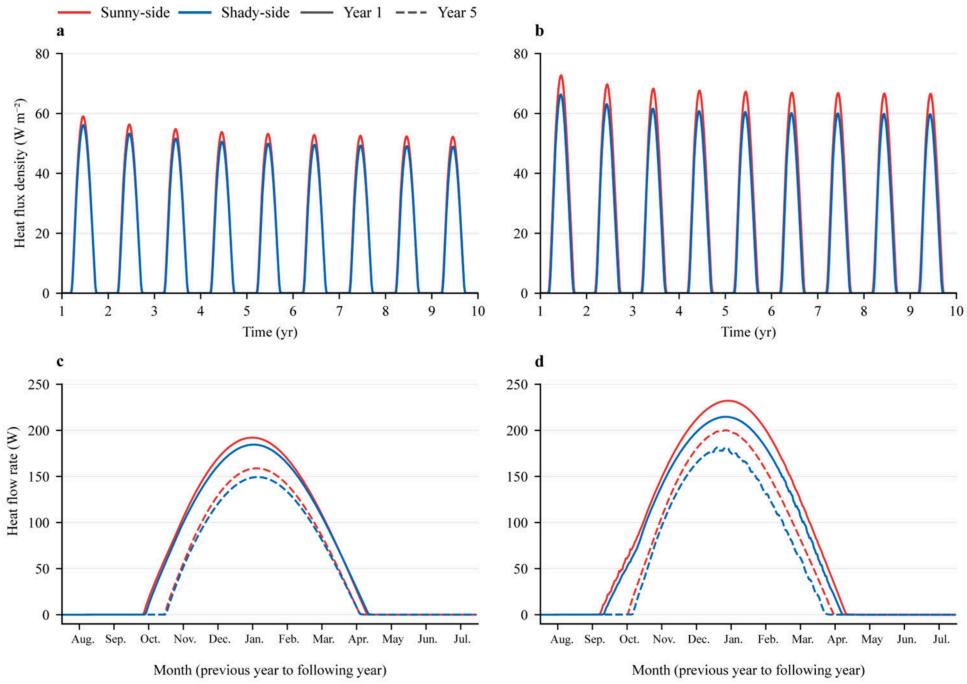


Figure 14. Operating responses of different TPCT configurations. (**a**,**b**) Heat flux density over years 1–10 for CIT and NHT; (**c**,**d**) heat flow rate in years 1 and 5 for CIT and NHT.

For the CIT, heat-flux-density peaks were approximately 60–65 W m^{-2} in year 1 and stabilized at about 50–55 W m^{-2} after year 10 (Figure 14a). For the NHT, the year-1 peaks reached approximately 75–80 W m^{-2} on the sunny side and about 65 W m^{-2} on the shaded side. After year 10, the NHT peaks remained at approximately 60–67 W m^{-2} (Figure 14b). Heat flow rate followed the same seasonal pattern (Figure 14c,d). The year-1 peak heat flow rate was higher than the year-5 value, and the NHT generally showed higher peak heat flow rates than the CIT under the same climatic forcing. This operating difference is consistent with the contact between the horizontal evaporator and the thermally disturbed basal zone beneath the embankment.

Figure 15 shows that TPCT operation was controlled by the effective temperature difference between the mean evaporator temperature and ambient air temperature. Start-up

occurred when cold-season air temperature became sufficiently lower than the evaporator temperature, and shut-down occurred as this temperature difference decreased during the warm season. As the soil around the evaporator cooled after construction, the effective operating duration shortened from year 1 to year 5 in both layouts. For the CIT, the operating durations of the sunny-side and shaded-side TPCTs decreased from 197 and 196 d in year 1 to 172 and 169 d in year 5, respectively. For the NHT, the corresponding durations decreased from 217 and 209 d to 181 and 171 d. The NHT therefore maintained a longer cold-season operating window than the CIT under the same climatic forcing, especially on the sunny side.

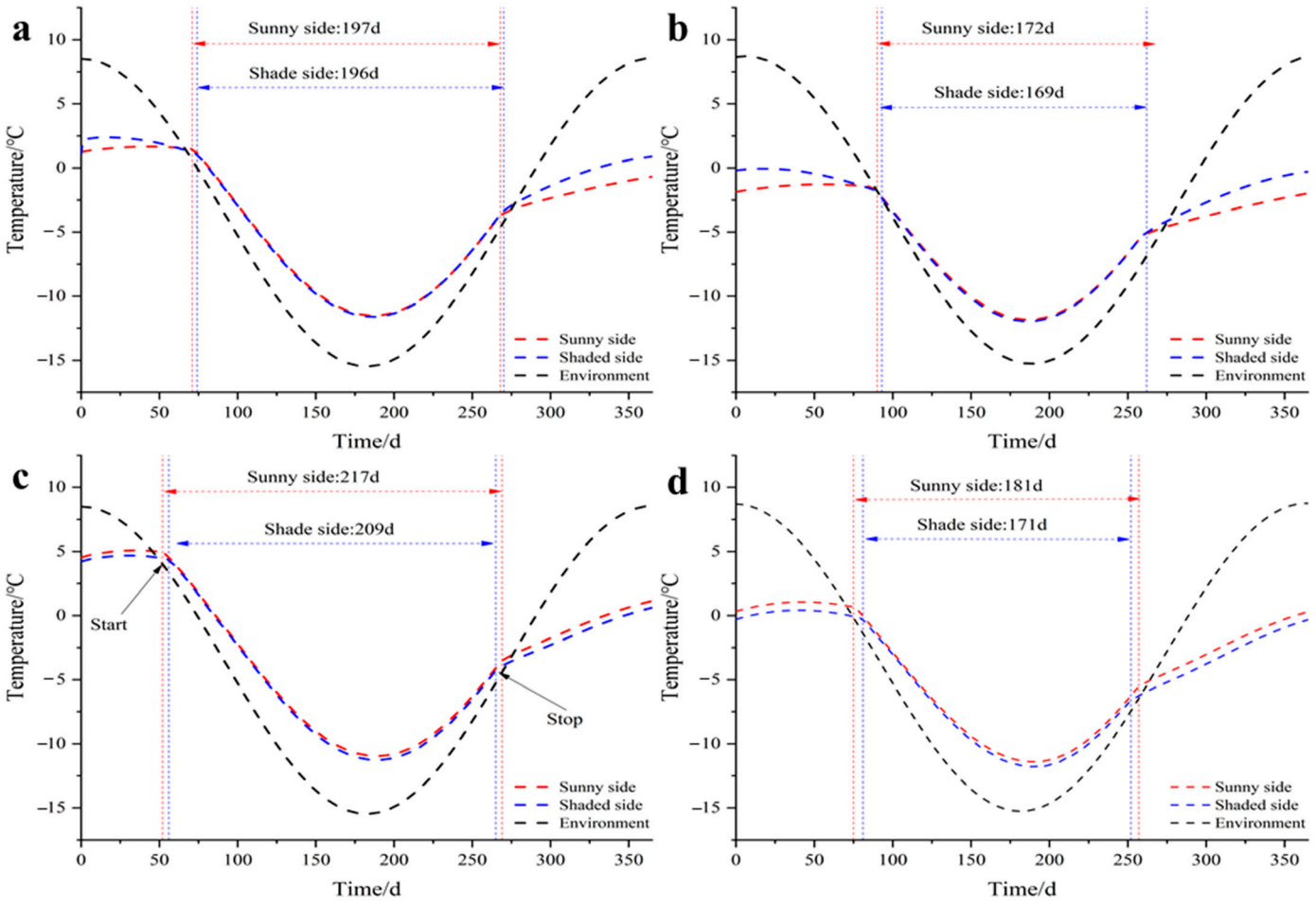


Figure 15. Annual effective operating duration of different TPCT configurations. (**a**,**b**) CIT in years 1 and 5; (**c**,**d**) NHT in years 1 and 5.

Cumulative cooling capacity helps explain the stronger shallow regulation produced by the horizontal layout (Figure 16). In both layouts, annual cumulative cooling capacity was highest in year 1, decreased rapidly during the early years, declined more slowly after year 5 and approached a stable level after year 10. For the CIT layout, annual cumulative cooling capacity decreased from 2060 to 1410 MJ on the sunny side and from 1990 to 1320 MJ on the shaded side between years 1 and 20. For the NHT layout, it decreased from 2650 to 1870 MJ and from approximately 2390 to 1600 MJ, respectively. The larger annual cumulative cooling capacity of the NHT was consistent with its longer operating duration and closer contact between the horizontal evaporator and the shallow thermally disturbed zone beneath the embankment.

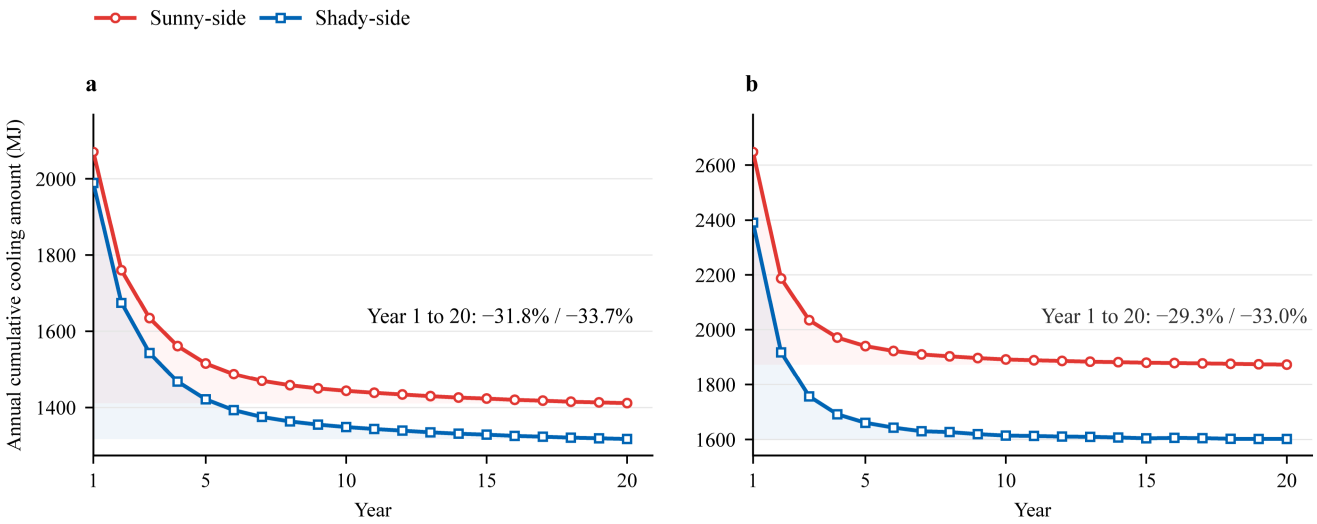


Figure 16. Effective cumulative cooling capacity of different TPCT configurations at different stages. (**a**) CIT; (**b**) NHT.

Appendix B provides an indirect magnitude check for the simulated TPCT operating responses using monitoring data from the Beiluhe TPCT test site. The monitored annual effective operating duration was approximately 165 d. Because heat-flux sensors were not installed on the TPCT wall, annual cooling capacity was estimated using the condenser-surface heat-transfer method and the cold-season averaged equivalent-thermal-resistance method. The two estimates were 1719.50 and 1547 MJ, respectively. These values are of the same order as reported annual cooling capacities of TPCT embankments on the Qinghai–Tibet Plateau (1480–1943 MJ) [18]. This comparison does not directly validate the NHT layout but suggests that the simulated TPCT operating responses are within a reasonable magnitude range.

3.5. Long-Term Differences in Temperature Uniformity and Layout Applicability

The long-term difference between the two layouts appeared most clearly in cross-sectional temperature uniformity and frozen-state continuity (Figure 17). At z = 0 m, near the natural ground surface and embankment-base level, the NHT maintained lower temperatures across most of the embankment influence zone. It also formed a laterally connected low-temperature belt beneath the embankment body. By contrast, the CIT showed stronger spatial fluctuation, with warmer segments between locally cooled zones. The horizontal evaporator was therefore better aligned with the shallow heat-entry zone created by the wide asphalt embankment.

At z = −4 m, the CIT produced lower local temperatures near the inclined evaporator influence zones, indicating stronger deep localized cooling. This cooling, however, was accompanied by pronounced lateral temperature gradients. The NHT produced a smoother lateral temperature profile at the same depth, although its local minimum temperature was higher than that of the CIT. The two profiles show that the CIT was more effective for deep local cooling, whereas the NHT provided better shallow lateral continuity and cross-sectional temperature uniformity.

Figure 18 compares the 20-year temperature variation at symmetric sunny-side and shaded-side positions within the TPCT cooling range. For the CIT, the sunny-side and shaded-side curves showed larger seasonal separation, especially during the cold season when localized cooling produced stronger temperature fluctuations (Figure 18a). For the NHT, the two curves remained closer throughout the simulation.

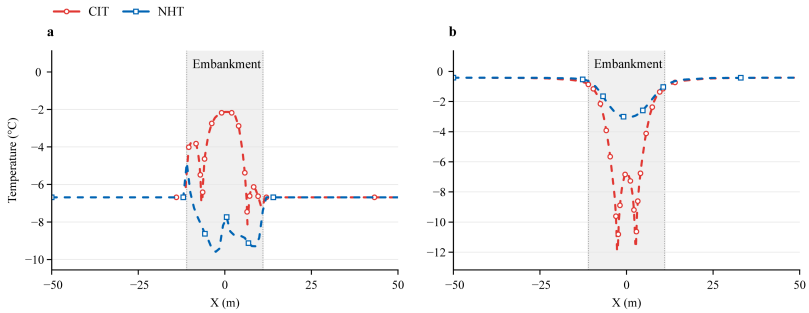


Figure 17. Lateral temperature distributions at the end of the cold season. (**a**) Year 10, z = 0 m; (**b**) year 10, z = −4 m.

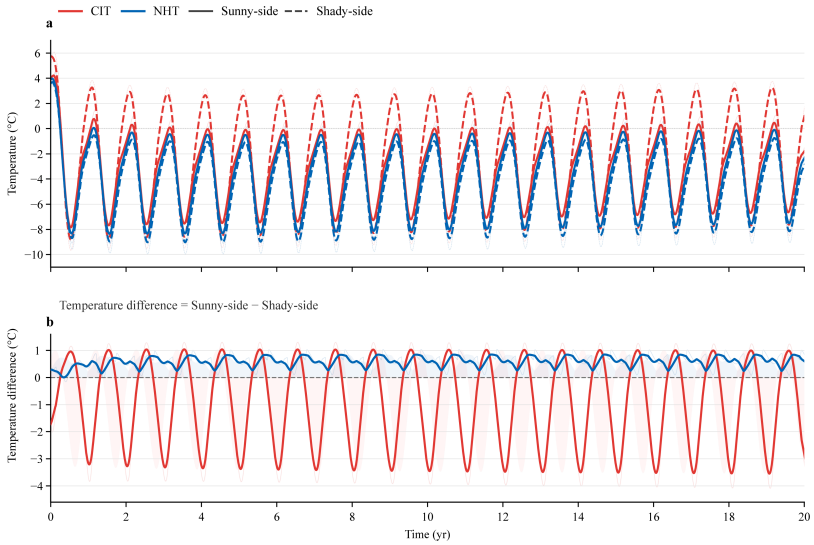


Figure 18. Sunny-shaded temperature asymmetry within the TPCT cooling range. (**a**) Temperature histories at symmetric sunny-side and shaded-side positions; (**b**) temperature difference between the sunny-side and shaded-side positions.

The temperature difference, defined as the sunny-side temperature minus the shaded-side temperature, quantifies the sunny-shaded asymmetry (Figure 18b). Under the CIT, the difference ranged from approximately −4.0 °C to 1.2 °C, reflecting localized cold anomalies and residual slope-aspect contrast. Under the NHT, the range narrowed to approximately 0–1.1 °C. The narrower range shows that the continuous horizontal evaporator reduced sunny-shaded thermal asymmetry within the shallow protected zone.

The CIT and NHT represent two embankment-scale cooling strategies rather than different intensities of the same measure. The CIT acts mainly as a deep localized cold source, producing strong cooling near the inclined evaporators and restraining deep thaw beneath the embankment body. Its influence, however, becomes less continuous toward the shoulders and slope toes [22]. The NHT acts mainly as a shallow continuous cold source, redistributing cooling along the embankment base and improving lateral temperature uniformity and ice-content continuity in the shallow foundation [34,36]. This distinction indicates that TPCT performance in wide asphalt embankments should be evaluated by frozen-zone geometry and residual weak-zone evolution, not only by local minimum temperature or maximum thaw depth.

The sunny-side slope toe remained the main residual weak zone after TPCT installation. The similar year-20 thaw depths at this location under the CIT and NHT layouts indicate that layout optimization alone cannot eliminate lateral boundary erosion. By contrast, the large thaw depth beneath the sunny-side shoulder in the no-TPCT case indicates a high hydrothermal potential for differential settlement, but not a direct structural

failure threshold. Roadbed failure also depends on traffic loading, consolidation and creep, which were not solved in this model [5,33]. For engineering practice, TPCT layout selection should therefore be combined with toe-focused auxiliary measures, such as local TPCT densification, additional toe TPCTs, crushed-rock protection, local insulation or drainage improvement [10,13,15].

The unified equivalent-resistance framework does not resolve inclination-dependent internal two-phase-flow resistance or long-term device ageing [28,29]. The equivalent surface-temperature boundary integrates radiation, wind convection, albedo and surface material effects, but does not explicitly solve full surface energy-balance feedbacks or nonlinear climate-acceleration scenarios [23]. The baseline validation used a representative standard year from long-term Beiluhe monitoring; short-term wind variability was represented by cold-season averaged equivalent heat-transfer conditions. Annual cooling capacity should therefore be interpreted as a reasonable magnitude range, not a fixed deterministic value. Future work should combine field monitoring, pipe-level energy measurements, surface energy-balance modelling and coupled hydrothermal-mechanical deformation analysis.

The two layouts also differ in construction applicability. Inclined TPCTs can be installed after embankment construction by drilling from the shoulder or slope region, making them suitable for existing embankments. Base-arranged novel horizontal TPCTs can be installed by horizontal drilling or laid directly at the embankment base during new construction, improving evaporator–soil contact but requiring earlier construction coordination and pipe protection. Galvanized TPCT condensers have operated on the Qinghai–Tibet Plateau for more than two decades without maintenance, suggesting that both layouts are practicable under normal service conditions. The horizontal phase-separated design, however, still requires field verification of long-term liquid-return stability. The frozen-state indicators used here are intended for layout comparison, not as universal design thresholds; warning values should be calibrated against site-specific settlement, pavement distress and serviceability data.

4. Conclusions

(1) Without thermosyphon protection, the wide asphalt embankment developed vertical and lateral degradation under the simulated warming condition. Thawing deepened beneath the pavement and embankment body, while thermal disturbance expanded toward the sunny-side slope. By year 20, the maximum thaw depth reached 10.06 m at the sunny-side shoulder and 9.76 m beneath the centerline, indicating that wide asphalt embankments require full cross-sectional assessment.

(2) Both TPCT layouts stabilized the 0 °C isotherm beneath the embankment body, but they produced distinct cooling geometries. The conventional inclined layout generated stronger, deep, localized cooling near the evaporators, whereas the base-arranged novel horizontal layout formed a more continuous, shallow cooling belt along the embankment. The TPCT performance in wide asphalt embankments depends on frozen-zone continuity and residual weak-zone evolution, not only on local minimum temperature or maximum thaw depth.

(3) Within the unified equivalent-resistance framework, the base-arranged novel horizontal layout maintained longer cold-season operation and higher annual cumulative cooling capacity in the wide embankment. In year 20, its annual cumulative cooling capacity reached 1870 MJ on the sunny side and 1600 MJ on the shaded side. The horizontal layout is more suitable for maintaining shallow frozen-state continuity across a wide embankment.

(4) The sunny-side slope toe remained the main residual weak zone after thermosyphon installation. TPCT layout selection should therefore be combined with toe-focused auxiliary protection, such as local thermosyphon densification, crushed-rock cooling, and insulation. For wide asphalt embankments, base-arranged novel horizontal TPCTs are more suitable when shallow lateral continuity is the priority, whereas inclined TPCTs remain useful when deep localized cooling is required.

Author Contributions: Conceptualization, J.W. and J.C.; methodology, J.W. and J.C.; software, J.W.; validation, J.W., T.D., S.Z. and X.H.; formal analysis, J.W.; investigation, J.W., X.H., J.Z. and Q.M.; resources, J.C., T.D., S.Z. and Y.W.; data curation, J.W. and J.Z.; writing—original draft preparation, J.W.; writing—review and editing, J.C., T.D., S.Z., X.H., J.Z., Q.M. and Y.W.; visualization, J.W.; supervision, J.C. and Q.M.; project administration, J.C.; funding acquisition, J.C. and Q.M. All authors have read and agreed to the published version of the manuscript.

Funding: This research was funded by the Research and Development Program of Science and Technology of China State Railway Group Co., Ltd., grant numbers K2024G010 and N2025Z003; the Science and Technology Research and Development Program of China Railway Qinghai–Tibet Group Co., Ltd., grant number QZ2025-G01; and the Science and Technology Foundation for Young Scientists of Gansu Province, grant number 24JRRA096.

Data Availability Statement: The data supporting the findings of this study, including model input parameters and simulation results, are available from the corresponding author upon reasonable request.

Acknowledgments: The authors thank Shandong Gaode Heat-transfer Equipment Co., Ltd. for providing relevant technical information on TPCT engineering.

Conflicts of Interest: Authors T.D. and S.Z. are employed by China Railway Qinghai–Tibet Group Co., Ltd. The remaining authors declare that the research was conducted in the absence of any commercial or financial relationships that could be construed as potential conflicts of interest.

Appendix A. Experimental Parameters and Monitoring Scheme of the TPCT

Table A1. Parameters of experimental test TPCT.

Item	Description
Pipe material	Carbon steel
Working fluid	Ammonia
Filling ratio	30%
Outer diameter	89 mm
Wall thickness	4.5 mm
Total length	2.1 m
Evaporator length	1.25 m
Adiabatic-section length	0.25 m
Condenser length	0.60 m
Inclination angles	0°, 30°, 60° and 90°
Number of trials	Each test condition was repeated twice
Condenser type	Smooth, finless tube
Steady-state criterion	Temperature variation < 0.1 °C and heat-flux variation < 5%
Constant temperature-difference test	Evaporator environment initially maintained at −1 °C; condenser environment decreased stepwise to −4, −7, −12 and −18 °C
Data acquisition frequency	1 measurement per minute
Steady-state data processing	Average values over the stable 10-min period after reaching steady state
Monitoring arrangement	Temperature sensors on evaporator, adiabatic and condenser sections; heat-flux sensors on evaporator and condenser sections
System heat loss	3%
Uncertainty treatment	Temperature sensor accuracy: ±0.05 °C; heat-flux sensor calibration error: 5%; system heat loss: 3%; estimated heat-transfer uncertainty: 6.82%

Appendix B. Field-Based Comparison of TPCT Operating Duration and Cooling Capacity

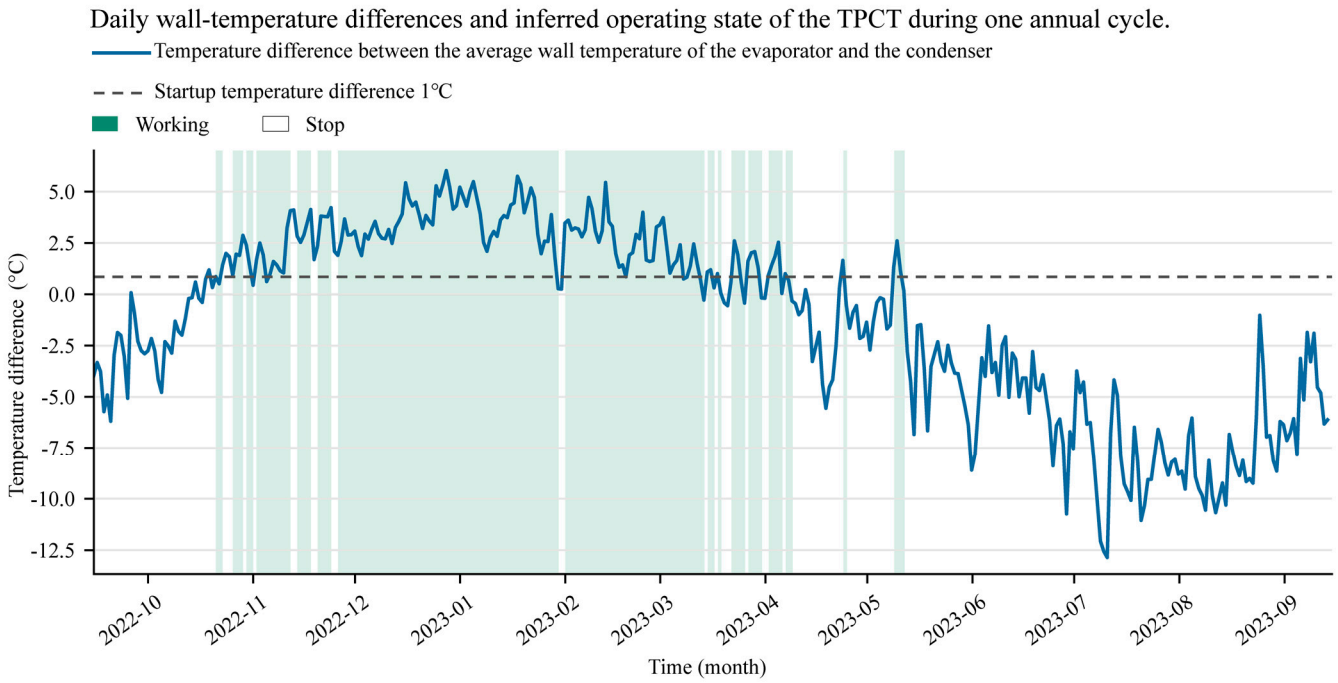


Figure A1. Daily wall-temperature differences and inferred operating state of the TPCT during one annual cycle.

Appendix B.1. Condenser-Surface Heat-Transfer Method

$$P_{total}(t) = P_{conv}(t) + P_{rad}(t)$$

$$P_{conv}(t) = h(t)A[T_{cond,wall}(t) - T_{air}(t)]$$

$$P_{rad}(t) = \varepsilon\sigma A[T_{c,K}(t)^4 - T_{a,K}(t)^4]$$

$$h(t) = 2.75 + 1.51v(t)^{0.2}$$

where $P_{total}(t)$ is the total heat-release power of the condenser at time t (W); $P_{conv}(t)$ is the convective heat-transfer power of the condenser at time t (W); $P_{rad}(t)$ is the radiative heat-transfer power of the condenser at time t (W); h(t) is the convective heat-transfer coefficient at time t (W m^{-2} K^{-1}); A is the external heat-transfer area of the condenser (m^2); $T_{cond,wall}(t)$ is the condenser-wall temperature at time t (°C); $T_{air}(t)$ is the air temperature at time t (°C); ε is the surface emissivity of the condenser (0.28); σ is the Stefan–Boltzmann constant, 5.67×10^{-8} W m^{-2} K^{-4}; $T_{c,K}(t)$ is the condenser-wall temperature in Kelvin at time t (K); $T_{a,K}(t)$ is the air temperature in Kelvin at time t (K); and v(t) is the wind speed at time t (m s^{-1}).

Using the monitored meteorological and TPCT wall-temperature data, the cumulative convective and radiative heat-transfer amounts were 1374.50 MJ and 345.00 MJ, respectively, giving a total annual condenser heat release of 1719.50 MJ.

Appendix B.2. Cold-Season Average Equivalent Thermal-Resistance Method

$$R_s = \ln(2r/D)/(2\pi\lambda L_e)$$

$$R_f = 1/(Ah)$$

where R_s is the thermal resistance between the evaporator and the surrounding soil (K W^{-1}); r is the effective cooling radius of the TPCT in the soil (m); D is the outer diameter of the TPCT evaporator (m); λ is the thermal conductivity of the surrounding soil (W m^{-1} K^{-1}); L_e is the evaporator length (m); R_f is the condenser-side heat-transfer resistance (K W^{-1}); A is the external heat-transfer area of the condenser (m^2); and h is the convective heat-transfer coefficient between the condenser surface and the ambient air (W m^{-2} K^{-1}).

The resulting cooling capacity was 1547 MJ.

Appendix B.3. Comparison with Published TPCT Cooling Capacity

These values are consistent with previously reported annual cooling capacities of TPCT embankments on the Qinghai–Tibet Plateau, which ranged from approximately 1480 to 1943 MJ during 2004–2012, mainly because of environmental variability.

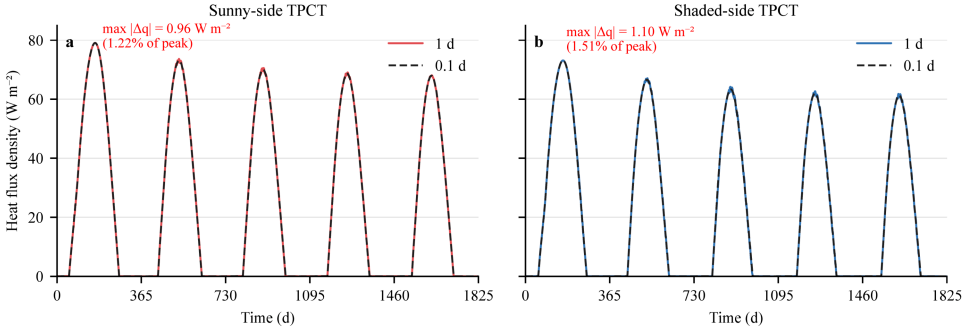


Figure A2. Time step sensitivity. (**a**) Sunny-side TPCT; (**b**) Shade-side TPCT.

Appendix C. Nomenclature

Table A2. Nomenclature.

Abbreviation/Symbol	Physical Meaning	Unit
TPCT	Two-phase closed thermosyphon	-
CIT	Conventional inclined two-phase closed thermosyphon	-
NHT	Base-arranged novel horizontal two-phase closed thermosyphon	-
XPS	Extruded polystyrene insulation layer	-
MAE	Mean absolute error	°C
RMSE	Root-mean-square error	°C
R^2	Coefficient of determination	Dimensionless
x, y, z	Transverse, longitudinal and vertical coordinates	m
T	Temperature	°C
t	Time	s, d or yr, as specified
C_e	Equivalent volumetric heat capacity	J m^{-3} K^{-1}
λ_e	Equivalent thermal conductivity	W m^{-1} K^{-1}
T_f	Characteristic freezing temperature	°C
ΔT	Phase-change smoothing interval	K
H_f	Phase-change smoothing function	Dimensionless
C_u, C_f	Specific heat capacities of thawed and frozen soil	J kg^{-1} K^{-1}
n	Soil porosity	m^3 m^{-3}
S	Degree of saturation	Dimensionless
ρ_s	Dry density of soil	kg m^{-3}

Table A2. *Cont.*

Abbreviation/Symbol	Physical Meaning	Unit
ρ_w	Density of water	kg m^{-3}
ρ_i	Density of ice	kg m^{-3}
L	Latent heat of ice–water phase change	J kg^{-1}
λ_u, λ_f	Thermal conductivities of thawed and frozen soil	W m^{-1} K^{-1}
θ_u	Volumetric unfrozen water content	m^3 m^{-3}
θ_i	Volumetric ice content	m^3 m^{-3}
θ_r	Residual volumetric water content	m^3 m^{-3}
θ_{tot}	Total volumetric water content	m^3 m^{-3}
q_w	Liquid-water flux	m s^{-1}
D_w	Moisture diffusion coefficient	m^2 s^{-1}
D_T	Temperature-gradient-driven moisture migration coefficient	m^2 s^{-1} K^{-1}
K_w	Hydraulic conductivity	m s^{-1}
a_1, b_1	Empirical parameters for unfrozen-water content	Dimensionless
a_2, b_2	Empirical parameters for hydraulic conductivity	m s^{-1}/dimensionless
a_3, b_3	Empirical parameters for water diffusivity	m^2 s^{-1}/dimensionless
n_{TPCT}	Outward unit normal vector of the evaporator boundary	Dimensionless
q_{TPCT}	Equivalent heat flux absorbed by TPCT evaporator	W m^{-2}
T_{evap}	Mean evaporator-wall temperature	°C
T_{air}	Ambient air temperature	°C
ΔT_{start}	TPCT start-up temperature difference	K
ΔT_{on}	Start-up smoothing interval	K
Q_{TPCT}	Heat-transfer power of a single TPCT	W
A_{eo}	Outer heat-exchange area of evaporator	m^2
R_{TPCT}	Equivalent total thermal resistance of TPCT	K W^{-1}
λ_{TPCT}	Thermal conductivity of TPCT pipe wall	W m^{-1} K^{-1}
L_e, L_c	Lengths of evaporator and condenser sections	m
d_o, d_i	Outer and inner diameters of TPCT	m
α_e	Boiling heat-transfer coefficient in evaporator	W m^{-2} K^{-1}
α_c	Condensation heat-transfer coefficient in condenser	W m^{-2} K^{-1}
A_e, A_c	Inner heat-exchange areas of evaporator and condenser	m^2
A_f	Effective outer heat-exchange area of finned condenser	m^2
T_0	Annual mean surface temperature	°C
A	Annual temperature amplitude in surface boundary	°C
φ	Initial phase of periodic temperature boundary	rad
ΔT_{air}	Climate-warming rate	°C yr^{-1}
q_g	Geothermal heat flux	W m^{-2}
χ_T	Empirical coefficient for temperature-gradient-driven moisture diffusion	Dimensionless

References

1. Biskaborn, B.; Smith, S.; Noetzli, J.; Matthes, H.; Vieira, G.; Streletskiy, D.; Schoeneich, P.; Romanovsky, V.; Lewkowicz, A.; Abramov, A. Permafrost Is Warming at a Global Scale. *Nat. Commun.* **2019**, *10*, 264. [CrossRef] [PubMed]
2. Hjort, J.; Streletskiy, D.; Doré, G.; Wu, Q.; Bjella, K.; Luoto, M. Impacts of Permafrost Degradation on Infrastructure. *Nat. Rev. Earth Environ.* **2022**, *3*, 24–38. [CrossRef]
3. Ran, Y.; Cheng, G.; Dong, Y.; Hjort, J.; Lovecraft, A.L.; Kang, S.; Tan, M.; Li, X. Permafrost Degradation Increases Risk and Large Future Costs of Infrastructure on the Third Pole. *Commun. Earth Environ.* **2022**, *3*, 238. [CrossRef]
4. Hansson, K.; Šimůnek, J.; Mizoguchi, M.; Lundin, L.; van Genuchten, M. Water Flow and Heat Transport in Frozen Soil: Numerical Solution and Freeze–Thaw Applications. *Vadose Zone J.* **2004**, *3*, 693–704. [CrossRef]
5. Yu, F.; Qi, J.; Lai, Y.; Sivasithamparam, N.; Yao, X.; Zhang, M.; Liu, Y.; Wu, G. Typical Embankment Settlement/Heave Patterns of the Qinghai–Tibet Highway in Permafrost Regions: Formation and Evolution. *Eng. Geol.* **2016**, *214*, 147–156. [CrossRef]

6. Liu, W.; Yu, W.; Hu, D.; Lu, Y.; Chen, L.; Yi, X.; Han, F. Crack Damage Investigation of Paved Highway Embankment in the Tibetan Plateau Permafrost Environments. *Cold Reg. Sci. Technol.* **2019**, *163*, 78–86. [CrossRef]
7. Yu, F.; Qi, J.; Yao, X.; Liu, Y. Comparison of Permafrost Degradation under Natural Ground Surfaces and Embankments of the Qinghai–Tibet Highway. *Cold Reg. Sci. Technol.* **2015**, *114*, 1–8. [CrossRef]
8. Zhang, M.; Pei, W.; Li, S.; Lu, J.; Jin, L. Experimental and Numerical Analyses of the Thermo-Mechanical Stability of an Embankment with Shady and Sunny Slopes in a Permafrost Region. *Appl. Therm. Eng.* **2017**, *127*, 1478–1487. [CrossRef]
9. Luo, X.; Yu, Q.; Ma, Q.; Guo, L. Study on the Heat and Deformation Characteristics of an Expressway Embankment with Shady and Sunny Slopes in Warm and Ice-Rich Permafrost Regions. *Transp. Geotech.* **2020**, *24*, 100390. [CrossRef]
10. Cheng, G.; Sun, Z.; Niu, F. Application of the Roadbed Cooling Approach in Qinghai–Tibet Railway Engineering. *Cold Reg. Sci. Technol.* **2008**, *53*, 241–258. [CrossRef]
11. Zhang, M.; Zhang, X.; Li, S.; Wu, D.; Pei, W.; Lai, Y. Evaluating the Cooling Performance of Crushed-Rock Interlayer Embankments with Unperforated and Perforated Ventilation Ducts in Permafrost Regions. *Energy* **2015**, *93*, 874–881. [CrossRef]
12. Liu, M.; Niu, F.; Ma, W.; Fang, J.; Lin, Z.; Luo, J. Experimental Investigation on the Enhanced Cooling Performance of a New Crushed-Rock Revetment Embankment in Warm Permafrost Regions. *Appl. Therm. Eng.* **2017**, *120*, 121–129. [CrossRef]
13. Luo, J.; Niu, F.; Liu, M.; Lin, Z.; Yin, G. Field Experimental Study on Long-Term Cooling and Deformation Characteristics of Crushed-Rock Revetment Embankment at the Qinghai–Tibet Railway. *Appl. Therm. Eng.* **2018**, *139*, 256–263. [CrossRef]
14. Ma, Q.; Luo, X.; Gao, J.; Sun, W.; Li, Y.; Lan, T. Numerical Evaluation for Cooling Performance of a Composite Measure on Expressway Embankment with Shady and Sunny Slopes in Permafrost Regions. *Energy* **2022**, *244*, 123194. [CrossRef]
15. Mei, Q.; Chen, J.; Wang, J.; Hou, X.; Zhao, J.; Zhang, S.; Dang, H.; Gao, J. Strengthening Effect of Crushed Rock Revetment and Thermosyphons in a Traditional Embankment in Permafrost Regions under Warming Climate. *Adv. Clim. Change Res.* **2021**, *12*, 66–75. [CrossRef]
16. Jafari, D.; Franco, A.; Filippeschi, S.; Di Marco, P. Two-Phase Closed Thermosyphons: A Review of Studies and Solar Applications. *Renew. Sustain. Energy Rev.* **2016**, *53*, 575–593. [CrossRef]
17. Song, Y.; Jin, L.; Zhang, J. In-Situ Study on Cooling Characteristics of Two-Phase Closed Thermosyphon Embankment of Qinghai–Tibet Highway in Permafrost Regions. *Cold Reg. Sci. Technol.* **2013**, *93*, 12–19. [CrossRef]
18. Wu, D.; Jin, L.; Peng, J.; Dong, Y.; Liu, Z. The Thermal Budget Evaluation of the Two-Phase Closed Thermosyphon Embankment of the Qinghai–Tibet Highway in Permafrost Regions. *Cold Reg. Sci. Technol.* **2014**, *103*, 115–122. [CrossRef]
19. Yu, F.; Qi, J.; Zhang, M.; Lai, Y.; Yao, X.; Liu, Y.; Wu, G. Cooling Performance of Two-Phase Closed Thermosyphons Installed at a Highway Embankment in Permafrost Regions. *Appl. Therm. Eng.* **2016**, *98*, 220–227. [CrossRef]
20. Luo, X.; Yu, Q.; Ma, Q.; You, Y.; Wang, J.; Wang, S. Evaluation on the Stability of Expressway Embankment Combined with L-Shaped Thermosyphons and Insulation Boards in Warm and Ice-Rich Permafrost Regions. *Transp. Geotech.* **2021**, *30*, 100633. [CrossRef]
21. Pei, W.; Zhang, M.; Yan, Z.; Lai, Y.; Lu, J.; Dai, Y. Thermal Control Performance of the Embankment with L-Shaped Thermosyphons and Insulations along the Gonghe-Yushu Highway. *Cold Reg. Sci. Technol.* **2022**, *194*, 103428. [CrossRef]
22. Yuan, C.; Yu, Q.; You, Y.; Guo, L. Formation Mechanism of Longitudinal Cracks in Expressway Embankments with Inclined Thermosyphons in Warm and Ice-Rich Permafrost Regions. *Appl. Therm. Eng.* **2018**, *133*, 21–32. [CrossRef]
23. Li, W.; Lin, Z.; Fan, X.; Yao, M.; Wu, X. Experimental Study on the Influence of Embankment Slope Direction on Near-Surface Thermal Conditions in Permafrost Region, Qinghai-Tibet Plateau. *Case Stud. Therm. Eng.* **2023**, *49*, 103311. [CrossRef]
24. Mei, Q.; Chen, J.; Zhao, J.; Hou, X.; Dong, T.; Zhang, S.; Zhao, Y.; Du, L. Long-Term Cooling Performance of Two-Phase Closed Thermosyphons in Warming Permafrost: A Field Case Study from the Qinghai–Tibet Railway. *Appl. Therm. Eng.* **2026**, *290*, 129980. [CrossRef]
25. Pei, W.; Zhang, M.; Li, S.; Lai, Y.; Jin, L.; Zhai, W.; Yu, F.; Lu, J. Geotemperature Control Performance of Two-Phase Closed Thermosyphons in the Shady and Sunny Slopes of an Embankment in a Permafrost Region. *Appl. Therm. Eng.* **2017**, *112*, 986–998. [CrossRef]
26. Ma, Q.; Lai, Y.; Luo, X.; Chen, H.; He, P.; Lin, X. Formation Mechanism and Characteristics of Longitudinal Cracking on Embankment with TPCTs in Permafrost Regions of the QTP. *Eng. Geol.* **2025**, *347*, 107927. [CrossRef]
27. Jiang, G.; Fu, Z.; Men, X.; Zhao, H.; Gao, S.; Liu, Y.; Wu, Q. Climate Warming Is Likely to Weaken the Performance of Two-Phase Closed Thermosyphon on the Qinghai–Tibet Plateau. *Adv. Clim. Change Res.* **2024**, *15*, 90–100. [CrossRef]
28. Wang, Y.; Wang, X.; Wang, J.; Liu, Y.; Chen, J. Heat Transfer Performance of a Two-Phase Closed Thermosyphon with Different Inclination Angles Based on the Core-Tube Monitoring. *Case Stud. Therm. Eng.* **2023**, *42*, 102738. [CrossRef]
29. Zhang, M.; Lai, Y.; Pei, W.; Jin, L. Effect of Inclination Angle on the Heat Transfer Performance of a Two-Phase Closed Thermosyphon under Low-Temperature Conditions. *J. Cold Reg. Eng.* **2014**, *28*, 04014007. [CrossRef]
30. Yan, Z.; Zhang, M.; Pei, W.; Li, D.; Chen, J.; Lai, Y. Effect of Length Ratios on the Cooling Performance of an Inclined Two-Phase Closed Thermosyphon under Negative Temperature Conditions. *Sol. Energy* **2020**, *204*, 600–616. [CrossRef]

31. Liu, Y.; Chen, J.; Wang, C.; Liu, Y.; Zhang, S.; Dong, T.; Zhao, Y.; Wang, J.; Wang, X.; Hou, X. Experimental Research on the Cooling Effect of a Novel Two-Phase Closed Thermosyphon with Semiconductor Refrigeration in Permafrost Regions. *Case Stud. Therm. Eng.* **2024**, *54*, 103935. [CrossRef]
32. Wang, G.; Lin, C.; Zhu, L.; Feng, D.; Xin, Y.; Zhang, F. Performance Analyses of Two-Phase Closed Thermosyphons for Road Embankments in the High-Latitude Permafrost Regions. *J. Mt. Sci.* **2023**, *20*, 3138–3153. [CrossRef]
33. Ma, Q.; Luo, X.; Gao, J.; Lan, T. Evaluation of the Application Effect of the Inclined TPCTs on an Embankment with the Shady-Sunny Slope Effect in Permafrost Regions. *Cold Reg. Sci. Technol.* **2023**, *213*, 103936. [CrossRef]
34. Chen, K.; Jin, M.; Li, G.; Liu, Y.; Lu, J.; Zhao, Y.; Yu, Q. Thermal Performance and Heat Transfer Process of an Expressway Embankment with Horizontal-Thermosyphons in Permafrost Regions. *Cold Reg. Sci. Technol.* **2023**, *212*, 103887. [CrossRef]
35. Pei, W.; Zhang, M.; Lai, Y.; Zhang, X.; Luo, T. A Self-Adaption Horizontal Thermosyphon Technology in Uneven Thermal Control of Roadway Embankments in Sub-Arctic Permafrost Regions. *Transp. Geotech.* **2022**, *33*, 100714. [CrossRef]
36. Jin, M.; Shang, K.; Yu, Q.; Chen, K.; Guo, L.; You, Y. Study on Working Performance and Cooling Effect of a Novel Horizontal Thermosyphon Applied to Expressway Embankment in Permafrost Regions. *Cold Reg. Sci. Technol.* **2024**, *221*, 104147. [CrossRef]
37. Zhou, Y.; Zhang, M.; Pei, W.; Wu, K.; Li, G. Numerical Modeling and Cooling Performance Evaluation of a Pressure-Driven Two-Phase Closed Thermosyphon with a Long Horizontal Evaporator. *Renew. Energy* **2024**, *222*, 119804. [CrossRef]
38. Chen, K.; Li, G.; Yu, Q.; You, Y.; Jin, M.; Lu, J.; Zhao, Y. Thermal Enhancement of Targeted Cooling Thermosyphon Array Applied to the Embankment–Bridge Transition Section of the Qinghai–Tibet Railway in Warm Permafrost. *Adv. Clim. Change Res.* **2024**, *15*, 1160–1176. [CrossRef]
39. Liu, S.; Shang, Y.; Lin, Z.; Wu, X.; Liu, L.; Liu, Y.; Li, W. In-Situ Monitoring Reveals the Energy Regulation Mechanism of Two-Phase Closed Thermosyphons in Wide Asphalt Highway Embankments in High-Altitude Permafrost Regions. *Energy* **2026**, *352*, 140966. [CrossRef]
40. Zhang, M.; Lai, Y.; Zhang, J.; Sun, Z. Numerical Study on Cooling Characteristics of Two-Phase Closed Thermosyphon Embankment in Permafrost Regions. *Cold Reg. Sci. Technol.* **2011**, *65*, 203–210. [CrossRef]
41. Xu, X. *Physics of Frozen Soil*; Science Press: Beijing, China, 2010.
42. Li, S.; Lai, Y.; Pei, W.; Zhang, S.; Zhong, H. Moisture–Temperature Changes and Freeze–Thaw Hazards on a Canal in Seasonally Frozen Regions. *Nat. Hazards* **2014**, *72*, 287–308. [CrossRef]
43. Li, S.; Zhang, M.; Pei, W.; Lai, Y. Experimental and Numerical Simulations on Heat-Water-Mechanics Interaction Mechanism in a Freezing Soil. *Appl. Therm. Eng.* **2018**, *132*, 209–220. [CrossRef]
44. Zhu, L. Study of the Adherent Layer on Different Types of Ground in Permafrost Regions on the Qinghai-Xizang Plateau. *J. Glaciol. Geocryol.* **1988**, *10*, 8–14.
45. Qin, D. *The Comprehensive Evaluating Report on the Environment Evolvement in West China*; Science Press: Beijing, China, 2002.

Disclaimer/Publisher's Note: The statements, opinions and data contained in all publications are solely those of the individual author(s) and contributor(s) and not of MDPI and/or the editor(s). MDPI and/or the editor(s) disclaim responsibility for any injury to people or property resulting from any ideas, methods, instructions or products referred to in the content.